



**HAL**  
open science

# Metabolite Profiling and Integrative Modeling Reveal Metabolic Constraints for Carbon Partitioning under Nitrogen-Starvation in the Green Alga *Haematococcus pluvialis*.

Lee Recht, Nadine Töpfer, Albert Batushansky, Noga Sikron, Aliza Zarka, Yves Y. Gibon, Zoran Nikoloski, Aaron Fait, Sammy Boussiba

## ► To cite this version:

Lee Recht, Nadine Töpfer, Albert Batushansky, Noga Sikron, Aliza Zarka, et al.. Metabolite Profiling and Integrative Modeling Reveal Metabolic Constraints for Carbon Partitioning under Nitrogen-Starvation in the Green Alga *Haematococcus pluvialis*.. *Journal of Biological Chemistry*, 2014, 289 (44), pp.30387-30403. 10.1074/jbc.M114.555144 . hal-02639565

**HAL Id: hal-02639565**

**<https://hal.inrae.fr/hal-02639565>**

Submitted on 28 May 2020

**HAL** is a multi-disciplinary open access archive for the deposit and dissemination of scientific research documents, whether they are published or not. The documents may come from teaching and research institutions in France or abroad, or from public or private research centers.

L'archive ouverte pluridisciplinaire **HAL**, est destinée au dépôt et à la diffusion de documents scientifiques de niveau recherche, publiés ou non, émanant des établissements d'enseignement et de recherche français ou étrangers, des laboratoires publics ou privés.

Copyright

# Metabolite Profiling and Integrative Modeling Reveal Metabolic Constraints for Carbon Partitioning under Nitrogen Starvation in the Green Algae *Haematococcus pluvialis*<sup>\*[5]</sup>

Received for publication, February 5, 2014, and in revised form, August 14, 2014. Published, JBC Papers in Press, September 2, 2014, DOI 10.1074/jbc.M114.555144

Lee Recht<sup>†1</sup>, Nadine Töpfer<sup>§1</sup>, Albert Batushansky<sup>‡</sup>, Noga Sikron<sup>‡</sup>, Yves Gibon<sup>¶</sup>, Aaron Fait<sup>‡</sup>, Zoran Nikoloski<sup>§</sup>, Sammy Boussiba<sup>‡2</sup>, and Aliza Zarka<sup>‡</sup>

From the <sup>‡</sup>French Associates Institute for Agriculture and Biotechnology, the Jacob Blaustein Institutes for Desert Research, Ben Gurion University of the Negev, Sede Boker 84990, Israel, the <sup>§</sup>Systems Biology and Mathematical Modeling Group, Max Planck Institute of Molecular Plant Physiology, Potsdam 14476, Germany, and the <sup>¶</sup>INRA, Université de Bordeaux, Bordeaux Metabolome Facility Bordeaux, UMR 1332 Fruit Biology and Pathology, Villenave d'Ornon 33140, France

**Background:** The microalga *H. pluvialis* shows a distinct pattern of carbon repartitioning upon nitrogen starvation.

**Results:** Data-driven integrative modeling pinpoints metabolic adjustments underlying carbon repartitioning.

**Conclusion:** *In vitro* and *in silico* experiments can dissect the systemic response to nitrogen starvation.

**Significance:** Experimental data in conjunction with integrative modeling enables model-driven hypothesis testing.

The green alga *Haematococcus pluvialis* accumulates large amounts of the antioxidant astaxanthin under inductive stress conditions, such as nitrogen starvation. The response to nitrogen starvation and high light leads to the accumulation of carbohydrates and fatty acids as well as increased activity of the tricarboxylic acid cycle. Although the behavior of individual pathways has been well investigated, little is known about the systemic effects of the stress response mechanism. Here we present time-resolved metabolite, enzyme activity, and physiological data that capture the metabolic response of *H. pluvialis* under nitrogen starvation and high light. The data were integrated into a putative genome-scale model of the green alga to *in silico* test hypotheses of underlying carbon partitioning. The model-based hypothesis testing reinforces the involvement of starch degradation to support fatty acid synthesis in the later stages of the stress response. In addition, our findings support a possible mechanism for the involvement of the increased activity of the tricarboxylic acid cycle in carbon repartitioning. Finally, the *in vitro* experiments and the *in silico* modeling presented here emphasize the predictive power of large scale integrative approaches to pinpoint metabolic adjustment to changing environments.

Photosynthetic algae use light energy and carbon dioxide (CO<sub>2</sub>) to generate and store chemical energy. Under imbalanced growth conditions, the carbon fixed by algae can be directed toward compounds serving as storage reserves (*e.g.* starch and lipids), which can be readily used to provide energy

and a carbon skeleton when needed (1–3). The composition of these reserve molecules depends on the environmental conditions and is interconnected with the content of other classes of metabolite compounds (*e.g.* carotenoids) (4, 5).

The freshwater green microalga *Haematococcus pluvialis* has been extensively studied due to its ability to accumulate the valuable secondary metabolite astaxanthin (6). This ketocarotenoid is a powerful antioxidant used as a food additive for humans and as a colorant in aquaculture (7). Different stress conditions, including high salinity, high irradiance, and nutrient deprivation, induce the accumulation of astaxanthin to up to 4% of the cell's dry biomass (8, 9). However, the highest rate of accumulation was observed under the combined stress of nitrogen starvation and high light (HL)<sup>3</sup> exposure (10). This accumulation is accompanied by massive morphological and metabolic changes (11), (*e.g.* the alga encysts and produces high amounts of carbohydrates (CHs) and fatty acids (FAs), which can reach up to 65 and 35% of the cell's dry biomass, respectively (6, 12). This behavior is unique in that most studied microalgae accumulate either FAs or CHs, but not both, when exposed to stress.

The temporal patterns of change in the cell's components upon nitrogen starvation and HL indicate that CH accumulation is an immediate response to the stress application, followed by FA accumulation (12), probably at the expense of the CHs. This observation suggests that the FAs are in part built from starch degradation derivatives. Similar results have been obtained in studies of species of the family Chlorellaceae; for instance, under sulfur deficiency, lipid accumulation begins with a reduction in stored starch (13), and in *Chlorella* UTEX29, the number of lipid bodies increased while starch granules decreased after 24 h of nitrogen deprivation (14).

<sup>\*</sup> This work was financially supported by the European Commission's Seventh Framework Program for Research and Technology Development (FP7) projects GIAPAP and BIOFAT.

<sup>[5]</sup> This article contains supplemental Information Sheets 1–7.

<sup>†</sup> Both authors contributed equally to this work.

<sup>2</sup> To whom correspondence should be addressed. Tel.: 972-8-6596795; Fax: 972-8-6596802; E-mail: sammy@bgu.ac.il.

<sup>3</sup> The abbreviations used are: HL, high light; CH, carbohydrate; FA, fatty acid; TAG, triacylglycerol; InDisMinimizer, integrated discrepancy minimizer;  $\mu$ E, microeinsteins; DW, dry weight; Chl, chlorophyll; TCH, total carbohydrate; FVA, flux variability analysis; Tcar, total carotenoid.

## Response of *H. pluvialis* Systems to Nitrogen Stress

Several studies have investigated the interplay of FA and CH biosynthesis and its regulation in microalgae, often with the aim of enhancing oil accumulation in the cell (15–20). For example, it was shown that inactivation of ADP-glucose pyrophosphorylase in a *Chlamydomonas* starchless mutant can lead to a 10-fold increase in triacylglycerol (TAG) (21); however, these findings are still being debated (3). Recently, increasing attention has been given to carbon partitioning under different stress conditions (12–14, 21). Nevertheless, the interplay between carbon pools in microalgae is not entirely resolved.

Furthermore, during the stress response *H. pluvialis* exhibits an increased activity of the tricarboxylic acid (TCA) cycle. For the green alga *Chlamydomonas reinhardtii* as well as plants, it has been proposed that FA biosynthesis can be promoted by the enhanced activity of the TCA cycle (22–24). Moreover, in *Hematococcus lacustris*, transcriptome analysis of the response to high irradiance and nutrient starvation revealed a general increase in respiration transcripts (*i.e.* glycolysis, TCA cycle, electron transport, phosphorylation) during astaxanthin accumulation (25). Although the TCA cycle is known to function as an essential component of the respiratory metabolism contributing to the generation of energy in the cell (26), its exact involvement in the stress response remains elusive.

The temporal changes in the cell's major components and activity patterns suggest concerted repartitioning of the carbon pools and activation of the TCA cycle in response to environmental cues. This observation of a system-wide response reinforces the need to provide a system-based understanding of the metabolic regulation and constraints involved in the response of *H. pluvialis* to stress. One promising approach to tackling this task is metabolic profiling, which provides a snapshot of the metabolic status of a cell. As endogenous (*e.g.* developmental cues) and exogenous (*e.g.* environmental cues) factors induce perturbations at the levels of gene expression, post-transcriptional/post-translational regulation, and enzyme activity, these processes lead to a concerted shift in the metabolic status of the cell. When integrated with enzyme data, metabolite profiling can reveal the activity in parts of the metabolic network (27). However, only a few investigations on metabolomic and enzymatic data integration have been conducted in microalgae (23, 28, 29), and a systems-based study of the carbon-nitrogen metabolism in response to nitrogen starvation under HL in *H. pluvialis* is still lacking.

In the present study, we explored the metabolic regulation and constraints of carbon partitioning under nitrogen starvation and HL in *H. pluvialis*. We integrated metabolite and enzyme activity data from *H. pluvialis* with the aim of generating a systems description of the microalga's metabolism. In addition, recent methodological developments have highlighted the possibility of predicting flux distributions and other molecular phenotypes by integrating experimental data with large scale metabolic models (30). We therefore developed a putative genome-scale model for *H. pluvialis* by extending the existing model of *Chlamydomonas* to allow the integration of data about the cell's physiology (*e.g.* FA, astaxanthin, and starch) and enzyme activities. The resulting genome-scale network reconstruction (31) was employed in combination with a novel constraint-based modeling approach termed integrated

discrepancy minimizer (InDisMinimizer) to investigate the following two questions. (i) Is starch degraded to supply carbon skeletons as precursors for the nitrogen starvation-induced FA synthesis? (ii) Does increased activity of the TCA cycle support FA biosynthesis? The results are discussed in the framework of the current knowledge on algal metabolism and its regulation under stress.

### EXPERIMENTAL PROCEDURES

**Organism and Growth Conditions**—*H. pluvialis* Flotow 1844em.Wille K-0084 was obtained from the Scandinavian Culture Center for Algae and Protozoa at the University of Copenhagen. The culture medium was BG-11 (32), modified according to Boussiba and Vonshak (6).

**Algal Cultures**—*H. pluvialis* was cultured as described previously (33). Cultures of green (non-flagellated) cells were first cultivated for 5 days in mBG-11 medium at an irradiance of  $75 \mu\text{E m}^{-2} \text{s}^{-1}$ . Exponentially growing cells were washed in double-distilled water and then resuspended in nitrogen-free mBG-11 medium at a concentration of  $2 \times 10^5$  cells  $\text{ml}^{-1}$ . To induce a rapid stress response to nitrogen depletion, cultures were exposed to a HL intensity of  $350 \mu\text{E m}^{-2} \text{s}^{-1}$  (10). The culture was held under these stress conditions for either 48 or 96 h, as specified below.

**Measurements of Growth Parameters and Pigment Content**—Samples were taken at 0, 6, 12, 24, 36, and 48 h after the stress application for the 48-h exposure and at 0, 24, 48, 72, and 96 h for the 96-h exposure to the stress conditions. The growth parameters: dry weight (DW), cell count, chlorophyll (Chl), and total carotenoid contents, were measured as described previously (6). However, DW determination was slightly modified, and the filters were dried in a microwave oven (Lenco model LMW-1826) at power level 3 for 8 min. Cell size was determined microscopically (Axioskop 1 (Zeiss) connected to an Olympus DP70 digital camera). Protein content was determined by the BCA method according to Smith *et al.* (34).

**Total Sugar Determination**—Total carbohydrate (TCH) content was determined by the anthrone method (35, 36) with specific modifications for *H. pluvialis* (12). Biomass (200  $\mu\text{g}$ ) was centrifuged at  $16,000 \times g$ , and the supernatant was discarded. Residues were then hydrolyzed in boiling  $\text{H}_2\text{SO}_4$  for 10 min. Once cooled to room temperature, 1 ml of anthrone reagent (35, 36) was added to all samples and incubated at room temperature for 30 min, and absorbance was read in a spectrophotometer at 625 nm. Samples were then quantified by comparison with a calibration curve made from glucose under the same conditions.

**Analysis of FA Composition and Content**—Transmethylation of biomass, and quantification and qualification of FAs were determined as described by Zhekisheva *et al.* (33). Transmethylation of FAs was performed by incubating freeze-dried biomass in dry methanol containing 2% (v/v)  $\text{H}_2\text{SO}_4$  at  $80^\circ\text{C}$  for 1.5 h under argon atmosphere and continuous stirring. Heptadecanoic acid (C17:0; Sigma-Aldrich) was added as an internal standard. FA methyl esters were quantified and qualified on a Trace GC Ultra (Thermo, Italy) equipped with flame ionization detector and programmed temperature vaporizing injector. The detector temperature was fixed at  $280^\circ\text{C}$ , and helium was

## Response of *H. pluvialis* Systems to Nitrogen Stress

used as the carrier gas. The programmed temperature vaporizing injector was programmed to increase the temperature from 40 °C at time of injection to 300 °C at time of sample transfer. Separation was achieved on a fused silica capillary column (ZB-WAX+, Phenomenex, 30 m × 0.32 mm). FA methyl esters were identified by co-chromatography with authentic standards (Sigma-Aldrich).

**Enzyme Activity Measurements**—For routine measurements, samples (~50 mg DW) were collected and centrifuged (4000 × g, for 5 min), supernatants were removed, and pellets were immediately frozen in liquid nitrogen and stored at −80 °C. Prior to extraction, samples were resuspended in extraction buffer (27) without detergent to prevent cell breakdown and were then subaliquoted into fractions of ~2 mg DW. After centrifugation (4000 × g, for 5 min), the supernatant was removed, and samples were ground and stored at −80 °C. Extraction was then performed as described by Gibon *et al.* (37). Enzyme activities were determined as follows: pyruvate kinase (EC 2.7.1.40) and phosphoenolpyruvate carboxylase (EC 4.1.1.31) according to Gibon *et al.* (27); citrate synthase (EC 2.3.3.1), NAD-dependent isocitrate dehydrogenase (EC 1.1.1.41), succinyl-CoA synthetase (EC 6.2.1.4), and NAD-dependent malate dehydrogenase (EC 1.1.1.37) according to Nunes-Nesi *et al.* (38); aconitase (EC 4.2.1.3) according to Piques *et al.* (39); and NADP-dependent malic enzyme (ME; EC 1.1.1.38) according to Gerrard Wheeler *et al.* (40). Measurements were performed for two different setups. In setup 1 (48 h), 10 enzymes were measured in two independent experiments (A and B) with four biological replicates each, and in setup 2 (96 h), 21 enzymes were measured in four independent experiments (C–F) with four biological replicates. A detailed list of the enzymes measured under each setup can be found in [supplemental Information Sheet 1](#).

**Sample Extraction for Metabolite Profiling**—Samples (~15 mg DW) were collected and centrifuged (4000 × g, for 5 min), and the supernatant was discarded. The cells were immediately frozen in liquid nitrogen and stored at −80 °C until extraction. Metabolite extraction followed an established protocol (41) optimized for algal cells. In short, samples were ground using a miniature bead beater (BioSpec Products Inc.) and 2.5-mm glass beads for 6 min with 700 μl of 100% methanol mixed with internal standard (8.4 μl of D-[UL-<sup>13</sup>C<sub>6</sub>]glucitol (Cortecnet Corp., catalogue no. ALD-053, from a stock of 10 mg ml<sup>−1</sup> for each sample)). Sorbitol was used instead of ribitol to enhance standard resolution. The samples were then centrifuged at 14,000 × g for 10 min. To separate the polar water-soluble phase from the apolar lipid phase, chloroform and double-distilled water were added to a final ratio of 1.5:1.4:0.75 water/methanol/chloroform, respectively. Samples were then centrifuged (4000 × g for 10 min), and 200 μl of the upper phase with methanol/water was moved to an Eppendorf tube and dried in a SpeedVac concentrator for 7 h at room temperature. Samples were then stored at −80 °C until analysis.

**Derivatization and Analysis of Primary Metabolites Using GC-MS**—Extracted material was derivatized by a GC-MS technique according to the protocol described by Lisec *et al.* (41). Chromatographic separation was carried out on a Thermo Scientific DSQ II gas chromatograph/mass spectrometer using a FactorFour Capillary VF-5ms column, and chromatograms

were analyzed using TagFinder04 software version 1.0 (42). Metabolites were annotated by comparison with mass spectra in the Golm database (43). All four biological replicates were analyzed for each condition.

**Multivariate and Statistical Analyses**—Prior to the analysis, data were normalized to the median of each metabolite over the entire sample set and log-transformed. Cluster analysis was performed based on the PAM (partitioning around medoids) algorithm (44) using the “cluster” package in the R statistical computing environment, version 3.0.2. The distance matrix was calculated by using  $1 - r^2$ , where  $r$  is the Pearson correlation coefficient. The number of clusters  $k$  was identified as the square root of  $n/2$ , where  $n$  is the total number of elements used (metabolites and enzymes). The compounds were ordered according to classes: enzymes, sugars and alcohols, amino acids and nitrogen compounds, carboxylic acids, others. Differences between means were tested for significance using Student's  $t$  test.

**Computational Approach**—The state of the art approach for modeling genome-scale network reconstruction is constraint-based optimization (*i.e.* flux balance analysis) (31). This method has the advantage that it only needs the stoichiometry of the participating reactions (represented in the stoichiometric matrix  $S$ ), lower and upper boundaries for the respective fluxes, and an optimization goal (*i.e.* objective, whose coefficients are captured in the vector  $c$ ) as input to predict steady-state flux distributions that are thermodynamically feasible and mass-balanced. No knowledge of initial metabolite concentrations or kinetic parameters is required. The generic problem formulation results in a linear program, which can be efficiently solved as follows.

$$\max c \cdot v \quad (\text{Eq. 1})$$

$$\text{s.t. } S \cdot v = 0 \quad (\text{Eq. 2})$$

$$v_{\text{lb}} \leq v \leq v_{\text{ub}} \quad (\text{Eq. 3})$$

To improve the predictive power, a large set of methods that integrate experimental data has been derived, which is described elsewhere (30). Below, we detail aspects of our modeling approach.

**Integration of the External Conditions**—The genome-scale model on which our analysis was based explicitly accounts for different light qualities and quantities (*i.e.* the effect of different light sources and intensities on the metabolic behavior of the cell can be simulated). For our *in silico* experiments, the light source was set to white fluorescent light with an intensity of 350 μE m<sup>−2</sup> s<sup>−1</sup>, according to the wet laboratory experiments. To approximate how much of the emitted photons are actually absorbed by the organism, we followed the approach presented by Chang *et al.* (45) and used an effective and dimensional photon flux conversion factor (see also [supplemental Information Sheet 2](#)). The effective photon flux conversion considers the fact that not all light incident on a cell is available for sustaining metabolism, but it may also be reflected or scattered. To approximate this factor, we compared the experimentally measured O<sub>2</sub> evolution in dependence of the light intensity with the simulated curve and found 80% of the maximum pho-

## Response of *H. pluvialis* Systems to Nitrogen Stress

tosynthetic activity to be achieved at  $\sim 1000 \mu\text{E m}^{-2} \text{s}^{-1}$  (46). The effective photon conversion factor was then determined as follows.

$$\text{Conversion}_{\text{Eff}} = \frac{145 \text{ mE/g DW/h}}{1000 \mu\text{E/m}^2/\text{s} \times \text{Conversion}_{\text{Dim}}} \\ = 0.0375 \text{ effective/incident photon flux} \quad (\text{Eq. 4})$$

The dimensional photon flux conversion factor includes cell parameters, such as cell diameter and DW. We explicitly accounted for cell growth during the stress application by deriving a time-dependent dimensional conversion factor, based on an approximated minimum and maximum cell diameter for each time point (see [supplemental Information Sheet 2](#)). The time-dependent dimensional photon flux conversion factor was then derived as follows.

$$\text{Conversion}_{\text{Dim}} = \frac{\text{cross-sectional area}}{\text{dry weight}} \times \frac{3600 \text{ s}}{\text{h}} \times \frac{1 \text{ mE}}{1000 \mu\text{E}} \quad (\text{Eq. 5})$$

To mimic internal nitrogen recycling during the nitrogen starvation stress, we allowed a maximum nitrogen uptake of 0.25e–7% of the upper flux boundary of the nitrogen-containing medium.

**Integration of Sink Reactions and Derivation of Experimental Flux Values**—We modeled the measured physiological parameters, including total carotenoid (Tcar), protein, TCH, Chl, and total fatty acid (TFA), as sums over several metabolites that were allowed to accumulate in the model. These metabolites were categorized into five groups: (i) astaxanthin (accumulation of other carotenoids can be neglected (11)); (ii) all 21 amino acids; (iii) carbohydrates (all sugars that form biomass in the model (*i.e.* mannose, arabinose, and galactose) as well as starch); (iv) Chl (Chl *a* and *b*); and (v) FAs. For the last group, we used all metabolites in the model that are associated with the metabolic pathways of “FA biosynthesis,” “FA elongation in mitochondria,” “FA metabolism,” and “biosynthesis of unsaturated FAs.” A complete list of all sink metabolites can be found in [supplemental Information Sheet 3](#). All physiological measurements (in  $\text{g liter}^{-1}$ ) were converted to rates ( $\text{mmol g DW}^{-1} \text{h}^{-1}$ ) as follows. We determined the mean value of all replicates of each experiment and divided it by the mean DW for each time point of the time course. For the compounds with unknown molecular weight, estimations were provided. For instance, for the protein content, we assumed an average number and molecular weight of amino acids per protein. The average molecular weight of the FAs was approximated by using measured ratios of the main FA constituents. A detailed list of the estimated ratios can be found in [supplemental Information Sheet 4](#). These values were then converted to rates by considering the changes between adjacent time points and calculating the mean value for each two adjacent rates. For the first time point, we used the rate determined from the data for the time points zero and one; for the last time point, we used the rate determined from the data for the second to last and last time point. Furthermore, we used the measured enzyme activity data as a proxy for the flux through the respective reaction.

**InDisMinimizer**—The derived time-dependent flux estimations were integrated by minimizing the discrepancy between data and predictions (InDisMinimizer). The problem definition results in the following quadratic optimization problem for each time point,

$$\min \sum_{i \in \text{measured}} \|\mathbf{E}_{i,t}\|_2^2 \quad (\text{Eq. 6})$$

$$\text{s.t. } S \cdot \mathbf{v}_t = 0 \quad (\text{Eq. 7})$$

$$\mathbf{v}_{\text{lb}} \leq \mathbf{v}_t \leq \mathbf{v}_{\text{ub}} \quad (\text{Eq. 8})$$

$$\mathbf{v}_{i,t} = \mathbf{v}_{i,t}^{\text{measured},t} + \mathbf{E}_{i,t} \quad (\text{Eq. 9})$$

where  $\mathbf{v}_t$  is the flux distribution at time  $t$ ;  $\mathbf{v}_{i,t}$ ,  $\mathbf{v}_{i,t}^{\text{measured}}$ , and  $\mathbf{E}_{i,t}$  are the predicted fluxes, the flux estimated from the data, and the corresponding error term for the reaction  $i \in \text{measured}$ , respectively, and  $\|\cdot\|_2^2$  denotes the second norm squared. Equation 7 gives the mass-balance constraints of the metabolic model, Equation 8 denotes the default lower and upper flux boundaries, and Equation 9 captures the relationship between the predicted and the estimated fluxes. The latter allows for an error term that might arise from experimental error or the errors in the derived rates. Because the flux constraints that were derived from the physiology data are 2 orders of magnitude lower than the flux constraints derived from the enzymology data, we introduced a relative weighting with an E-scaling factor of 100. In doing so, we ensured that all deviations between data and predictions are weighted equally. Moreover, our problem formulation assumed a steady state at each time point. Because the integrated data cover a time period of 0–96 h after the shift in nutrients and light intensity, we can assume that the system is in a pseudoequilibrium. This is based on the observation that metabolic changes usually happen on a minute time scale (47). The commercial solver MINOS was used to solve the resulting quadratic optimization problems.

**Flux Variability Analysis (FVA)**—FVA (48) is an approach that allows determination of the variability of the predicted fluxes for a given flux balance analysis solution. To this end, the lower and upper flux values for each reaction of the network under consideration are determined while still imposing the original constraints and the optimal value for the used objective. The resulting values provide a range of flux values for each reaction of the network that is compliant with the overall constraints. Therefore, on the one hand, FVA can assess the extent to which a predicted flux distribution can be used in testing and verifying a hypothesis. For instance, if the flux range of a reversible reaction of interest is between 1 and 2, we know that the reaction can only proceed in the forward direction, whereas, if we observe a flux range between –1 and 2, we cannot rule out the possibility that the reaction proceeds in the backward direction. On the other hand, results from FVA provide insights into flux capacities exhibited by a single reaction or pathway under given constraints. One application is to test the influence of one parameter in the model on a reaction of interest. For example, if changing a certain nutrient’s uptake rate results in a larger upper flux value for a reaction of interest, there exists a positive

influence of the increased uptake rate on the maximum flux through that reaction.

**Variability Flux Sampling**—Flux Variability Analysis is a useful tool to determine upper and lower flux values for reactions of interest, but it cannot be used to make statements about the likelihood of a certain flux value to be achieved. To address this problem, we here use a novel approach, termed variability flux sampling, in which we compute probability distributions of flux values based on a random flux value sampling. The method consists of two steps. First, for all reactions of interest, we randomly chose a flux value from the previously determined FVA interval. Because the fluxes are mutually dependent, one cannot guarantee that the set of randomly selected flux values for these reactions fulfills the optimality requirement or even the steady-state constraint. Therefore, in the second step, we use the previously determined constraints (*i.e.* optimality with respect to the minimized discrepancy from the data integration and steady state) together with the randomly selected set of flux values from the first step, and we minimize the Euclidian distance between the sampled set of flux values and a feasible set of flux values. In other words, given a randomly chosen set of flux values within the feasible flux boundaries, we determine a set of *feasible* flux values that is closest to the *random* set and fulfills the optimality constraints. Repeating this procedure many times results in a distribution of flux values for every reaction. The corresponding optimization problem can be cast as a quadratic problem with non-linear constraints,

$$\min \sum_{j \in R} \|\epsilon_{j,t}\|_2^2 \quad (\text{Eq. 10})$$

$$\text{s.t. } S \cdot v_t = 0 \quad (\text{Eq. 11})$$

$$v_{lb} \leq v_t \leq v_{ub} \quad (\text{Eq. 12})$$

$$v_{i,t} = v_{i,t}^{\text{measured},t} + E_{i,t} \quad \forall i \in M \quad (\text{Eq. 13})$$

$$\sum_{i \in M} \|E_{i,t}\|_2^2 = \text{MinDist}_t \quad (\text{Eq. 14})$$

$$v_{j,t} = v_{j,t}^{r,t} + \epsilon_{j,t} \quad \forall j \in R, \quad (\text{Eq. 15})$$

where Equations 11–13 are the constraints from the InDisMinimizer, Equation 14 assures overall optimality with respect to the results from the InDisMinimizer, and Equation 15 describes the relationship between the randomly sampled flux  $v_{j,t}^{r,t}$ , the feasible flux  $v_{j,t}$ , and the deviation term  $\epsilon_{j,t}$ , where  $R$  denotes the set of reactions for which randomized flux values are sampled from the corresponding FVA intervals. Note the difference between the error term  $E$  which describes the deviations from the experimental data, and the deviation term  $\epsilon$ , which denotes the deviation from the randomly sampled flux value. For the set of the seven reactions of interest, we repeated this analysis 20 times for every time point and each experiment, resulting in altogether 3200 sampling and optimization steps.

## RESULTS

### Changes in Metabolic Status Caused by Nitrogen Starvation under HL

Cultures of 5-day-old vegetative green *H. pluvialis* cells were inoculated into a nitrogen-free medium under continuous light

of  $350 \mu\text{E m}^{-2} \text{s}^{-1}$ . The combination of nitrogen deprivation and HL exposure was used to facilitate stress response (10). Cells were harvested every 6 or 12 h throughout the 48 or 96 h of exposure to stress. Metabolite data were only collected throughout the 48-h experiments, and the results of the physiological, metabolite, and enzyme activity data for these experiments are described below.

At time 0, the non-flagellated round palmelloid had an average diameter of  $24.7 \mu\text{m}$ . During the 48 h of stress, cells transformed into red cysts, and their average diameter increased to  $36.5 \mu\text{m}$  ( $p < 0.001$ ). Their number remained stable at  $2.5 \times 10^5$  cells  $\text{ml}^{-1}$  ( $p = 0.625$ ) throughout the experiment. The DW increased significantly ( $p < 0.001$ ) from  $0.5 \text{ g liter}^{-1}$  at time 0 to  $1.9 \text{ g liter}^{-1}$  after 48 h (Fig. 1A). Chl content remained stable at  $12 \text{ mg liter}^{-1}$  for the first 12 h and then decreased significantly ( $p < 0.001$ ) to  $6.1 \text{ mg liter}^{-1}$  after 48 h (Fig. 1A). Volumetric protein content (Fig. 1B) remained stable at  $0.13 \text{ g liter}^{-1}$  throughout the whole experiment; however, as an outcome of the increase in DW, the relative protein content in biomass decreased strongly ( $p = 0.012$ ) from 28 to 10.8% of DW during the first 12 h and then slowly but significantly to 7% ( $p = 0.006$ ) after 48 h (Fig. 1C). As reported previously (12), TCH content peaked after 24 h ( $p = 0.004$ ) both in volumetric (from  $0.2 \text{ g liter}^{-1}$  at time 0 to  $1.2 \text{ g liter}^{-1}$  after 24 h) and relative content (from 40% of DW at time 0 to 74% after 24 h). However, after 36 h, TCH content had decreased significantly ( $p = 0.020$ ) (to  $1 \text{ g liter}^{-1}$  and 54% of DW) and remained at this level throughout the rest of the experiment. TFA content gradually increased from 8% of DW at time 0 to 13% after 24 h ( $p = 0.012$ ) and further to 28% after 48 h ( $p = 0.014$ ) (Fig. 1C). Tcar content increased ( $p < 0.001$ ) from  $2.4 \text{ mg liter}^{-1}$  (0.6% of DW) at time 0 to  $76.5 \text{ mg liter}^{-1}$  (4.2% of DW) after 48 h (Fig. 2A). The major carotenoids at time 0 in *H. pluvialis* were lutein,  $\beta$ -carotene, violaxanthin, and neoxanthin, which amounted to 48.7, 21.3, 21.2, and 8.8% of Tcar, respectively (Fig. 2B). After 6 h of exposure to nitrogen starvation and HL stress, carotenoid composition changed dramatically with a strong increase ( $p < 0.001$ ) in astaxanthin content from 0 to 45.4% of Tcar, whereas all other major carotenoids decreased ( $p < 0.001$ ) by half. After 24 h of stress, astaxanthin content dominated carotenoid composition with 92.6% of Tcar and after 48 h reached 97.7% of Tcar (Fig. 2B).

To dissect the central metabolic processes and carbon partitioning to FA metabolism in response to nitrogen starvation under HL, samples were analyzed by an established GC-MS protocol and GC-flame ionization detector. We identified altogether 63 FAs and metabolites of the central metabolism (Fig. 3; for detailed values, see [supplemental Information Sheet 1](#)).

All sugar metabolites gradually increased after stress application, with the exception of maltotriose and raffinose, which peaked after 12 h of stress exposure and then gradually decreased. Maltotriose, a starch degradation product, significantly ( $p < 0.001$ ) increased 4.5-fold during the first 12 h and then significantly ( $p < 0.001$ ) decreased to its original content after 24 h and further to 0.7-fold its initial content after 48 h ( $p = 0.041$ ). Raffinose increased significantly ( $p < 0.001$ ) 10-fold within the first 12 h; however, after 24 h, it decreased strongly ( $p < 0.001$ ) to half its peak content and continued

## Response of *H. pluvialis* Systems to Nitrogen Stress

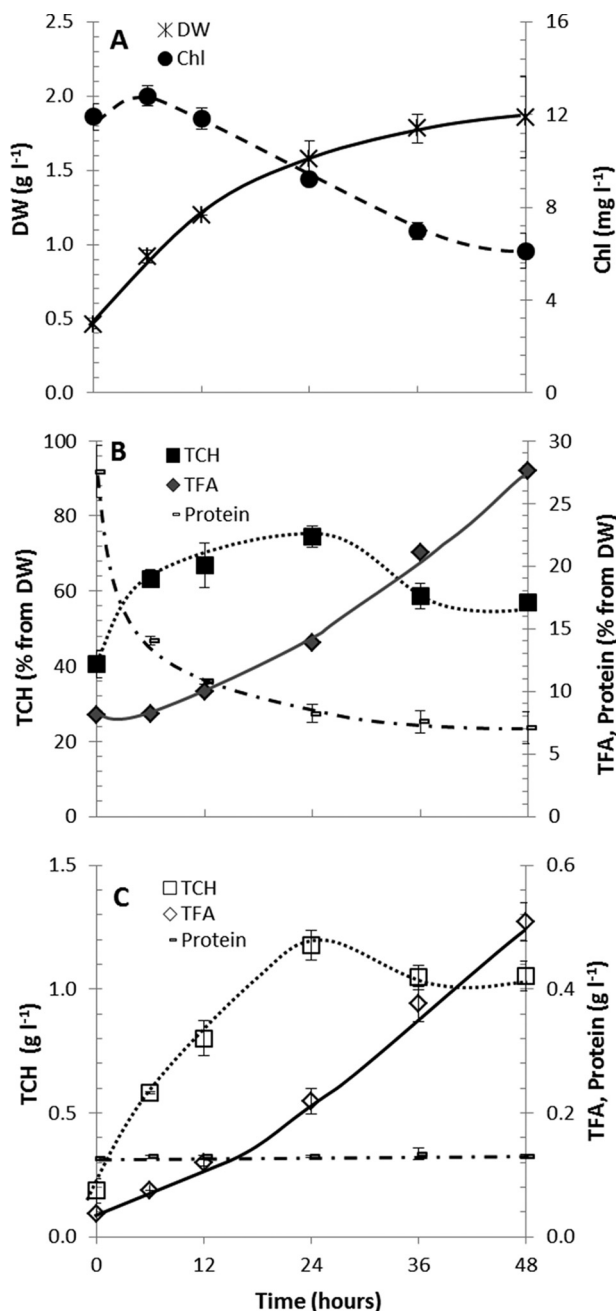


FIGURE 1. Changes in *H. pluvialis* cultures under nitrogen starvation and high light stress for 48 h. A, cell DW and chlorophyll. B, TFA, TCH, and protein contents in volumetric units. C, as in B but reported as relative contents.

decreasing ( $p = 0.019$ ) to 3.6-fold its initial value after 48 h (Fig. 3). Glycerol content increased significantly ( $p = 0.003$ ), peaking after 24 h with a -fold change of 35.6, and remained high for the following 24 h, in accordance with the observed TFA accumulation (Figs. 1 and 3).

Within the first 6 h, the content of the amino acids Lys, Pro, and Thr decreased significantly to 0.35-fold ( $p = 0.005$ ), 0.68-fold ( $p = 0.016$ ), and 0.56-fold ( $p = 0.014$ ) their initial values, respectively; however, after 12 h, the levels returned to their original values and in some cases even increased further (Fig. 3). Other amino acids, including Met, Cys, and Asn, significantly increased, with -fold changes of 6.6 ( $p = 0.007$ ), 15.3 ( $p =$

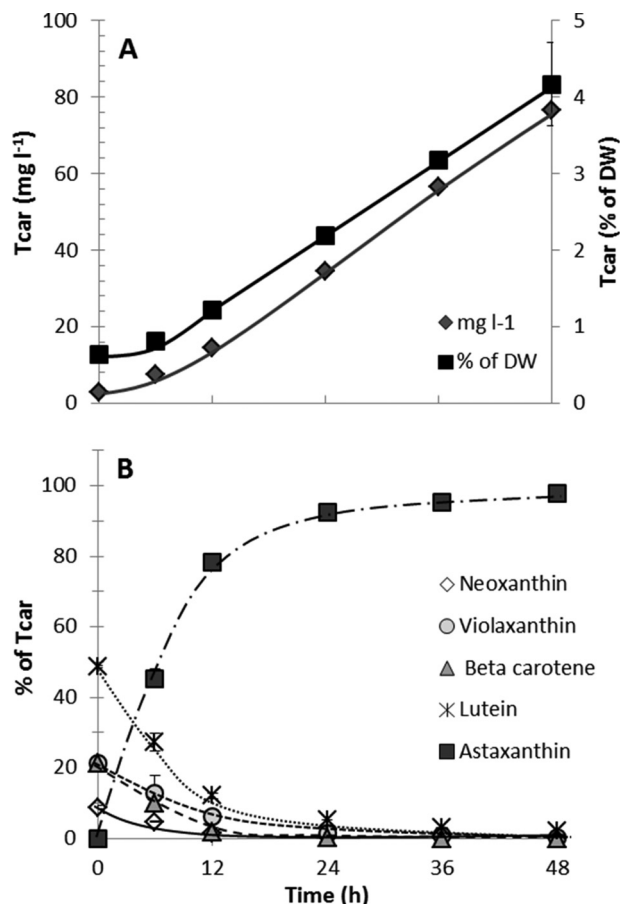


FIGURE 2. Changes in carotenoid content under nitrogen starvation and high light stress in *H. pluvialis* throughout 48 h. A, Tcar in volumetric and relative content. B, carotenoid composition presented as a percentage from Tcar.

0.025), and 8.2 ( $p < 0.001$ ), respectively, after 48 h of stress exposure (Fig. 3). Glu and Asp showed a decrease after 6 h to 0.2-fold ( $p < 0.001$ ) and 0.19-fold ( $p = 0.015$ ) their initial content, respectively. After 12 h, Glu remained at 0.4-fold its initial content, whereas Asp increased slightly ( $p = 0.013$ ) and eventually reached 0.64-fold its initial content. Remarkably, GABA showed the strongest increase with a -fold change of 5.5 after 6 h ( $p = 0.015$ ), 44.9 after 24 h ( $p = 0.015$ ), and 59.3 ( $p = 0.012$ ) after 48 h (Figs. 3 and 4).

FAs generally increased during the 48 h of stress exposure, and changes in composition occurred. The most significant increase was observed in oleic acid (C18:1w9), with a -fold change of 33.8 after 24 h ( $p = 0.013$ ) and a total -fold change of 99.6 after 48 h ( $p = 0.005$ ) (Fig. 3 and Table 1).

Enzyme activities were measured to further explore the alterations in the central carbon-nitrogen metabolism (Fig. 4). The patterns of change in both enzyme activity and metabolite abundance indicated a general enhancement of the TCA cycle and of the metabolic processes closely associated with it. Nevertheless, the TCA cycle did not act as one coherent unit; rather, different patterns were evident. The first pattern included phosphoenolpyruvate carboxylase, ME, and malate dehydrogenase, which all increased in activity during the first 12 h, followed by a decrease after 36 h and a subsequent activity peak after 48 h (Fig. 4). For example, ME activity increased

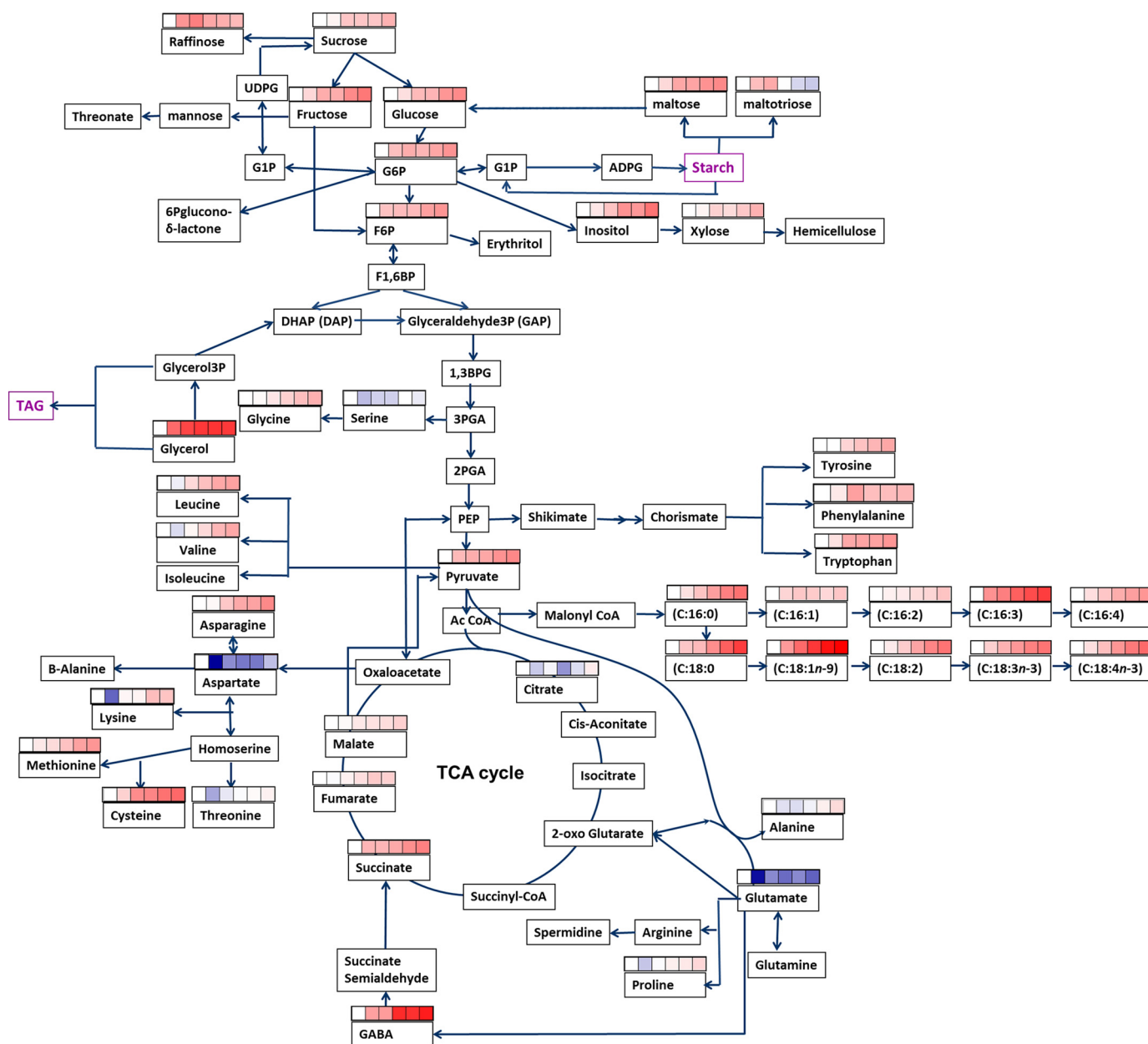


FIGURE 3. Simplified scheme of the major carbon-nitrogen metabolism in *H. pluvialis* and the changes in identified metabolites and fatty acids throughout 48 h of nitrogen starvation and high light. -Fold changes are represented as heat maps. Increase (red) and decrease (blue) in the cellular metabolite's content are indicated. Time points from left to right are 0, 6, 12, 24, 36, and 48 h.

significantly with a -fold change of 4 ( $p = 0.008$ ) during the first 12 h and then decreased to a -fold change of 1.5 ( $p = 0.011$ ) after 36 h and increased again to a -fold change of 6.9 ( $p < 0.001$ ) after 48 h. The metabolites associated with these enzymes included pyruvate and the TCA cycle intermediates malate, fumarate, and succinate. Pyruvate increased stepwise with -fold changes of 3.6 after 6 h ( $p = 0.025$ ) and 8.5 after 36 h ( $p = 0.012$ ). Malate gradually increased ( $p < 0.001$ ) throughout the experiment, with a 2.4-fold change after 48 h. Fumarate and succinate exhibited a response pattern similar to that of malate, with a strong accumulation of succinate up to a level of 10 times its initial content after 48 h ( $p = 0.006$ ).

The second pattern observed included citrate synthase and aconitase. The activity of both enzymes increased gradually

( $p < 0.001$ ) in the first 36 h and peaked after 48 h ( $p < 0.001$ ). Citrate, the intermediate metabolite between citrate synthase and aconitase, decreased significantly to 0.5-fold its initial content within the first 24 h ( $p = 0.002$ ) and subsequently returned to its initial level after 48 h.

The activity of succinyl-CoA synthetase remained stable during the first 36 h and then slightly but significantly increased after 48 h ( $p = 0.009$ ), hardly explaining succinate's response pattern. Isocitrate dehydrogenase activity remained constant during the first 12 h of stress exposure and then increased, with a -fold change of 2.8 after 24 h ( $p = 0.003$ ), followed by a decrease to a -fold change of 1.4 after 36 h ( $p < 0.001$ ) and then another increase to 2.9-fold of its initial value after 48 h ( $p = 0.002$ ).

## Response of *H. pluvialis* Systems to Nitrogen Stress

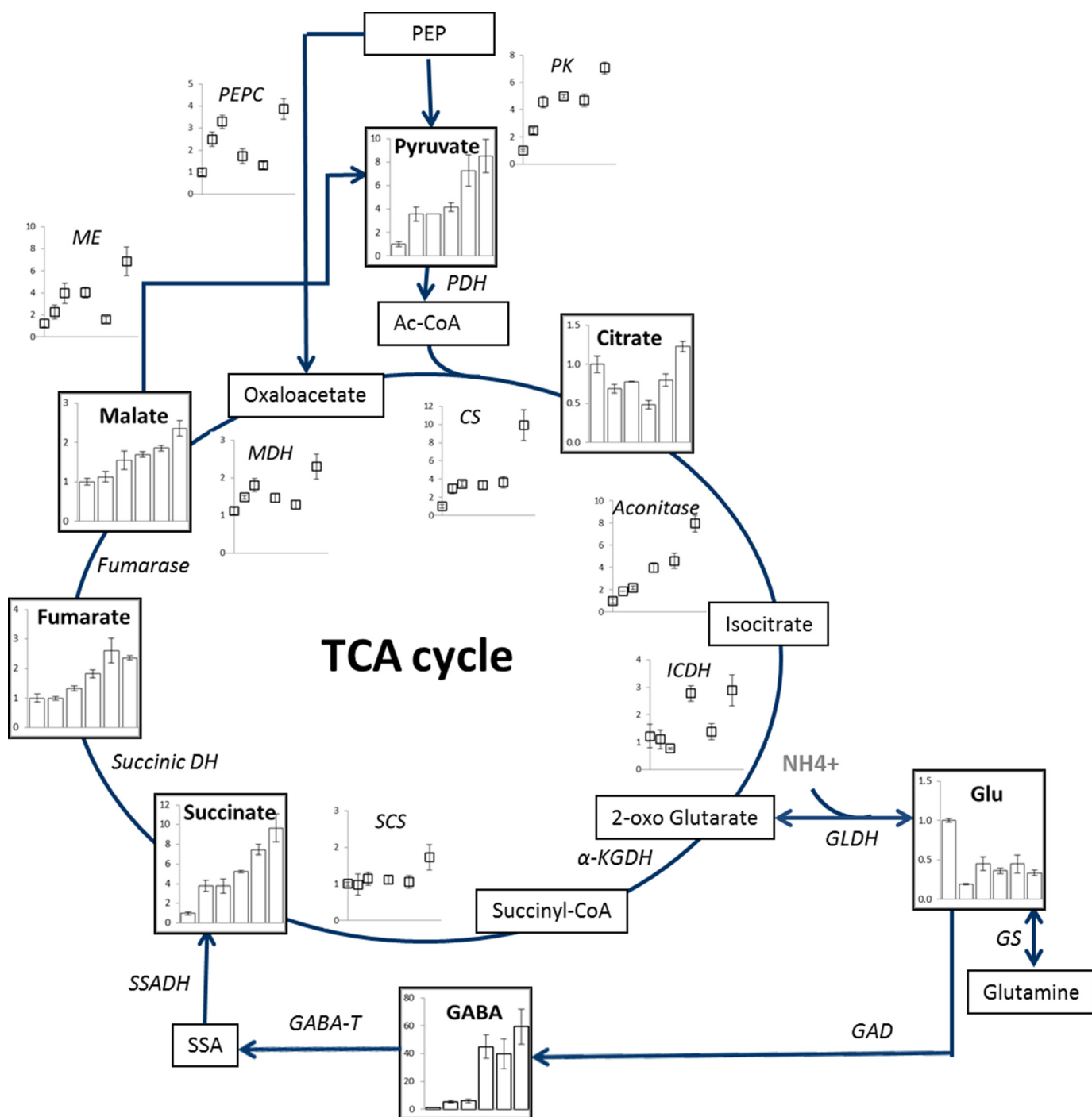


FIGURE 4. Changes in identified TCA cycle intermediates in *H. pluvialis* throughout 48 h of nitrogen starvation and high light. -Fold changes in metabolite content are represented as bar charts, and enzyme activities are shown as scatter charts. Time points from left to right are 0, 6, 12, 24, 36, and 48 h.

**TABLE 1**

### Changes in major fatty acid composition in *H. pluvialis* under nitrogen starvation and high light stress

Shown are -fold changes in fatty acid (lipid number nomenclature) content with respect to time 0. Values are normalized by cell number.

Time	Fatty acid composition								
	16:0	16:1	16:3	16:4	18:1w9	18:2	18:3w6	18:3w3	18:4w3
<i>h</i>									
0	1 ± 0.05	1 ± 0.00	1 ± 0.08	1 ± 0.02	1 ± 0.16	1 ± 0.03	1 ± 0.03	1 ± 0.01	1 ± 0.01
6	1.8 ± 0.04	1.4 ± 0.06	7.5 ± 0.3	1.9 ± 0.01	6.5 ± 0.18	1.5 ± 0.02	2.4 ± 0.17	2.5 ± 0.01	1.9 ± 0.07
12	3.3 ± 0.04	1.4 ± 0.04	11.4 ± 0.37	3.2 ± 0.00	16.2 ± 0.04	2.9 ± 0.01	3.4 ± 0.08	4.5 ± 0.00	3.7 ± 0.02
24	5.4 ± 1.06	1.0 ± 0.40	17.0 ± 1.70	4.2 ± 0.91	33.8 ± 5.43	4.9 ± 1.03	4.6 ± 0.66	6.1 ± 0.80	6.4 ± 1.02
36	8.4 ± 0.34	0.6 ± 0.12	21.5 ± 0.75	4.9 ± 0.18	60.2 ± 2.16	7.8 ± 0.26	5.7 ± 0.13	8.2 ± 0.21	9.4 ± 0.29
48	13.4 ± 0.63	0.9 ± 0.16	32.7 ± 1.24	6.9 ± 0.35	99.6 ± 4.91	12.8 ± 0.61	8.9 ± 0.44	12.9 ± 0.58	15.1 ± 0.71

### Integrated Cluster Analysis of the Enzyme Activity and Metabolite Data

Integrating two data sets generated from different analytical platforms is a challenge that can produce biologically inconsistent results (49). Nevertheless, it is one of the available tools to suggest potentially common behavior and underlying mechanisms of regulation. To test the occurrence of statistically coordinated patterns of change, cluster analysis was applied to the metabolite and enzyme activity data sets following the PAM algorithm (see [supplemental Information Sheet 5](#)). The cluster analysis resulted in five clusters of low average silhouette indices (a clustering quality measure), indicating a relatively weak affiliation of the elements with their respective cluster. The only cluster displaying a relatively high silhouette index (cluster 3) included metabolites that increased in content during the 48-h period and included non-glycolysis sugars, nitrogen-rich compounds, and the TCA cycle intermediates fumarate and malate. Interestingly, the only enzyme included in this cluster was aconitase, a TCA cycle enzyme driving the conversion of citrate to isocitrate via *cis*-aconitate. Despite its lower silhouette index, cluster 2 showed a coordinated pattern of change between pyruvate kinase (the enzyme producing pyruvate, the final product of glycolysis, on the one hand, and the precursor of acetyl-CoA, the main supplier of carbon to the TCA cycle, on the other hand), glycolysis sugars, the TCA cycle intermediate succinate, and pyruvate itself. Clusters 4 and 5, with relatively low silhouette indices and a small number of members, displayed a close biochemical relationship. Asp, Glu (cluster 5), and Ala (cluster 4) showed a similar pattern of change throughout the experiment. So did Thr (cluster 4), Ser (cluster 5), the branched-chain amino acid Val (cluster 4), and Asp-derived Lys (cluster 4), except for the last time point. These amino acids are closely connected biochemically. Cluster 1 was composed of enzymes with the exception of one sugar, alcohol xylitol.

### Model Development and Constraint-based Data Integration

Integration of experimental data in large scale metabolic models enables prediction and investigation of different molecular phenotypes (see Lewis *et al.* (30) for a recent comprehensive review). Here, we first described the model's development and how we integrated the available physiological and enzyme activity data. We then used the model and the proposed data integration approach to investigate biological questions of interest. Because the genome of *H. pluvialis* has not yet been assembled, we relied on modifying a recently published reconstruction of *Chlamydomonas*, a model green alga of the same order (45). Considering the list of pathways in MetaCyc (50) that are associated with *Chlamydomonas* and those that are associated with *Hematococcus*, we find an overlap of 99.4%; therefore, the model serves as a good starting point for the study. Moreover, the genome-scale model explicitly accounts for different light qualities and light quantities. To enable the integration of physiological characteristics specific for *H. pluvialis*, we included the astaxanthin pathway (see [supplemental Information Sheet 6](#)), based on MetaCyc (50), and introduced sink reactions for the measured physiological parameters

(e.g. CH and FA; see "Experimental Procedures" and [supplemental Information Sheet 3](#)). This manually curated putative model of the metabolism of *H. pluvialis* included 1975 metabolites and 2622 reactions, of which 422 are sink reactions for metabolites that are shown to accumulate during the stress response.

We used two types of data to constrain the obtained model: (i) parameters that describe the cell's environment (*i.e.* the experimental conditions) and (ii) measured physiological and enzyme activity data, which we used to derive experimental flux values (see "Experimental Procedures"). By integrating these two types of experimental data, we were able to, on the one hand, constrain fluxes into major biomass components and, on the other hand, specifically constrain flux bounds of core enzymes of the central carbon metabolism.

We set the light quality and quantity in the model to adequately describe the experimental setting. Because the geometric parameters of the cell changed significantly during the stress application (see "Changes in Metabolic Status Caused by Nitrogen Starvation under HL"), this needed to be explicitly considered when modeling the light absorption. We accounted for this change in morphology by deriving a time-dependent dimensional conversion factor, based on an approximated minimum and maximum cell diameter for each time point (see "Experimental Procedures" and [supplemental Information Sheet 2](#)). Nitrogen starvation was modeled as follows. Free nitrogen uptake was limited to time point zero; for all other time points, nitrogen uptake was blocked, and only internal nitrogen recycling was allowed (see "Experimental Procedures" for details of the implementation).

In the next step, to predict biologically meaningful flux distributions, we minimized the discrepancy between experimentally estimated and predicted fluxes by using the InDisMinimizer approach. To this end, we minimized the discrepancy, defined as the sum of squared weighted differences between all experimentally derived and predicted fluxes, quantifying the prediction error. For a detailed description of the computational approach, see "Experimental Procedures" and the schematic overview in Fig. 5.

Altogether, we applied the InDisMinimizer to six different biological replicates, each with four technical repeats. Experiments A and B (setup 1) were monitored for 48 h and comprised a set of 10 enzymes; experiments C–F (setup 2) were 96-h time series comprising 21 enzymes. For a list of the measured enzymes in both setups, see [supplemental Information Sheet 7](#). By using the proposed approach, we found a total error of between  $0.352 \times 10^{-3}$  and  $2.99 \times 10^{-3}$  for each time series and over all six experiments. To illustrate the agreement, Fig. 6 shows the experimentally derived and predicted fluxes for all measured enzymes and physiological parameters for experiment C. All predicted fluxes for reactions catalyzed by the measured enzymes could be reproduced with high accuracy; moreover, for all physiological parameters, except for the TCH curve at the second and third time points, we found a good fit. The fitted curves for the remaining experiments were of similar quality.

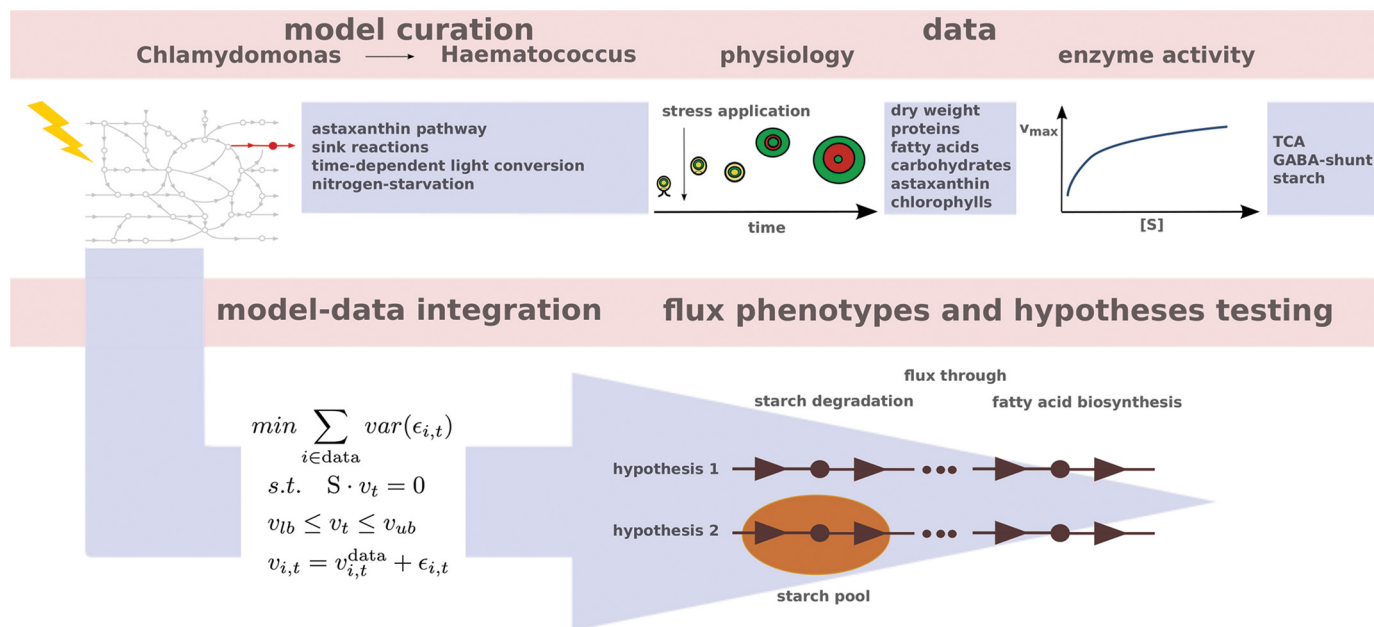


FIGURE 5. **Schematic representation of the computational approach.** Enzyme activity and metabolite data describing major physiological parameters were measured during the time course of the experiment. A putative metabolic model for *H. pluvialis* was curated based on an existing model of *Chlamydomonas*. The astaxanthin pathway, sink reactions for the integration of accumulating metabolites, and parameters describing the experimental setup were included. The data-model integration was performed by minimizing the discrepancy between experimentally derived and predicted fluxes. Based on this setup, several biological hypotheses can be tested, and alternative scenarios can be ruled out.

### Flux Variability

To assess the predictive power of our approach, we next performed FVA (48) for the same experiments. This method allows determination of the variability of the fluxes from a flux balance analysis solution by determining the minimum and maximum flux through a given reaction that results in the same optimal solution (*i.e.* minimum prediction error). If the integration of different types of experimental data leads to less varying fluxes than just one type of data or the generic flux bounds, the model is better constrained and therefore of higher predictive power. For instance, if two pathways lead to the same product, which is accumulated at a certain rate, integrating measured flux values for one pathway also narrows down the allowable flux range for the second pathway. The results of the FVA and S.D. values over all time points are given in Fig. 7. We divided the reactions into four groups: those that showed little ( $<100 \text{ mmol g DW}^{-1} \text{ h}^{-1}$ ), moderate ( $100\text{--}500 \text{ mmol g DW}^{-1} \text{ h}^{-1}$ ), high ( $500\text{--}1000 \text{ mmol g DW}^{-1} \text{ h}^{-1}$ ), and very high ( $>1000 \text{ mmol g DW}^{-1} \text{ h}^{-1}$ ) variability. For all six time points, we found more than 43% of all reactions to have low variability, indicating that the network is well constrained by the experimental data. We found between 33 and 39, 14 and 17, and 1 and 3% of the reactions to be in the second, third, and fourth groups, respectively.

We repeated the analysis by only integrating the physiological or enzyme activity data. Here we found only 32–35 and 35–37% of all reactions to be in the first group, respectively (Fig. 7). These results demonstrate the increase in predictive power by integrating two types of data (global parameters, such as TFA, TCH, and protein content, and activity rates of single enzymes) and allow the use of this approach in model-based testing of hypotheses. Moreover, the close fit between data and predictions further illustrates the suitability of the model *Chla-*

*mydomonas* reconstruction to capture metabolic behavior that is unique for *Hematococcus*.

### Model-based Hypothesis Testing

**Carbon Redistribution from Starch to FAs**—We used our setup to answer two biological questions. First, we addressed the question of whether starch degradation can yield precursors for *de novo* synthesis of FAs during the later stress response, a hypothesis proposed by Recht *et al.* (12). We applied the InDisMinimizer to two different scenarios, as illustrated in Fig. 5. Scenario 1 allowed for starch accumulation into a virtual pool over all time points; in addition, for the time points that showed starch degradation in the experiment, we also allowed for starch degradation into the system from the virtual pool. Scenario 2 also allowed for starch accumulation at all time points but not for starch degradation from the virtual pool back into the system. Here, starch was only allowed to exit the cell without being recycled into other building blocks. Fig. 8 shows the overall discrepancy between the data and the simulation as a sum over all time points for each biological replicate. *Dark* and *light green* represent scenarios 1 and 2, respectively. For all four replicates, scenario 1, which allowed for starch degradation, had a better fit, thus confirming the hypothesis that starch degradation is used to support FA synthesis during the second part of the stress response. Note that although the discrepancy was small in both cases, scenario 1 had, on average, a 3.3% better fit than scenario 2 for the two setups (*i.e.* 48 and 96 h). This average value also included the initial time points when neither scenario allowed for starch degradation from the virtual pool and, therefore, had the same discrepancy value. Considering the fact that altogether five physiological parameters as well as 10 or 21 enzymes (for setups 1 and 2, respectively) were fitted,

## Comparison of fluxes from experiment and simulation in mmol/gDWh

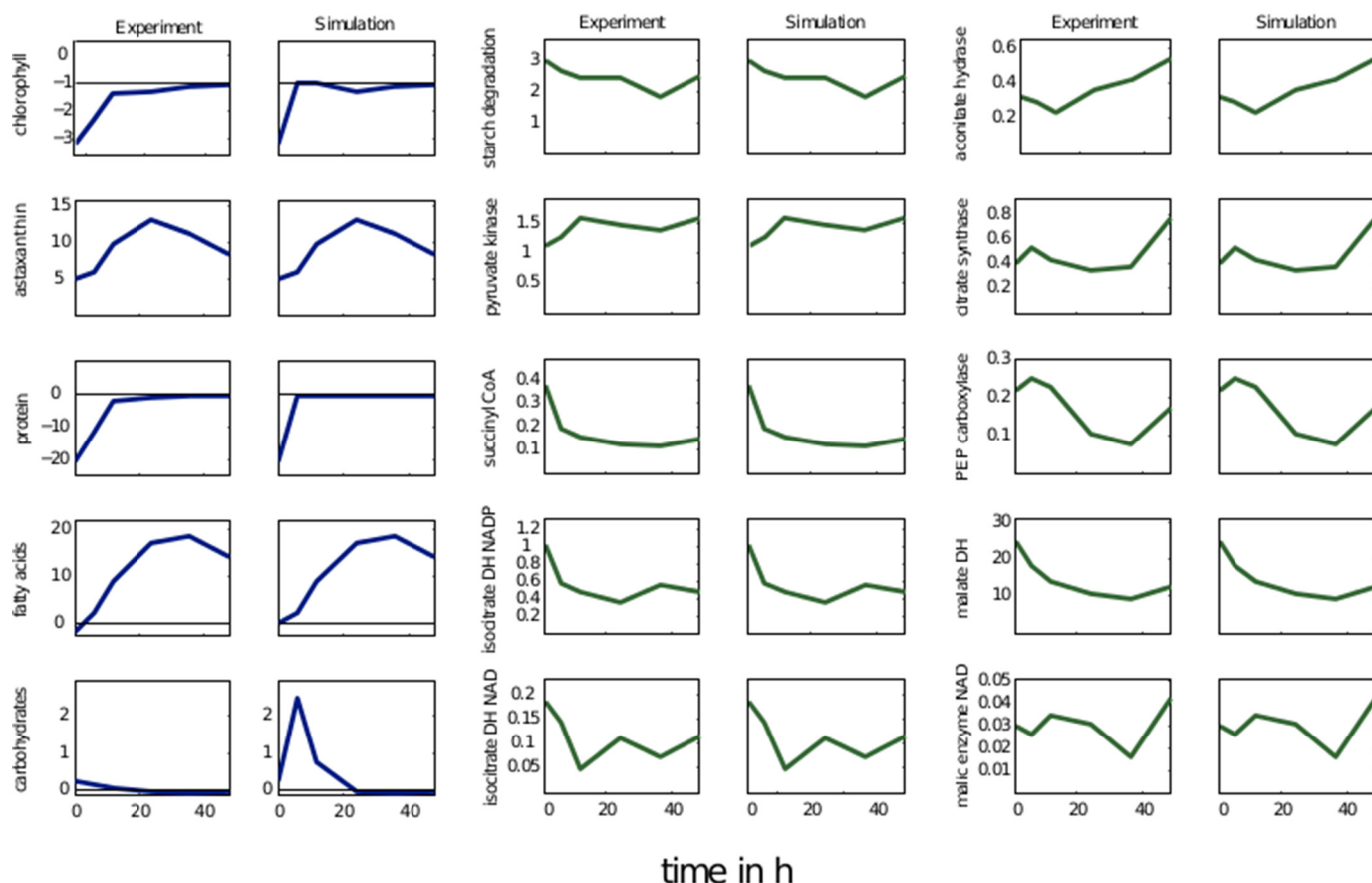


FIGURE 6. Results of the integrated discrepancy minimizer for experiment C. The model was used to determine flux distributions that minimize the weighted, squared difference between measured and predicted fluxes. Shown are the time series of the experimentally derived and predicted fluxes for all physiological parameters and all enzymes measured. Left panels, the rate for the experiment (Experiment). Right panels, the predicted rate in mmol g DW<sup>-1</sup> h<sup>-1</sup> (Simulation).

the increase in quality of the fit can be regarded as considerable. Furthermore, it is interesting to note that for setup 1 (*i.e.* 48 h), which is constrained by partly different enzyme activity data, the fits for scenario 1 performed over 5% better than those for scenario 2.

To further validate the hypothesis, we investigated three flux distributions based on the results of the InDisMinimizer. In this second step, we kept the determined minimum discrepancy between data and prediction fixed. Based on this overall best fit, we investigated (i) the variability of the flux through malonyl-CoA, the first reaction of the FA biosynthesis pathway; (ii) the variability of the flux for the sum of fluxes through the entire FA pathway; and (iii) the minimum discrepancy between the data and simulation for the FA biosynthesis. For the latter, we kept the best fit from the InDisMinimizer, and within the space of optimal flux distributions, we chose those that gave the best fit with respect to FA biosynthesis. The results of these computations are shown in Fig. 9. Bar plots in Fig. 9, A and B, are based on the difference in flux variability between scenarios 1 and 2 (*i.e.* scenario 1 – scenario 2) in percentage of the total flux variability with respect to scenario 1 and present the average over the time points at which starch degradation was observed in the experiment. The figure illustrates that for all experiments, both the first reaction of the pathway and the whole

pathway itself had larger flux variability in scenario 1 than in scenario 2, indicating that released building blocks from starch degradation enable a larger flux through the FA pathways. These findings highlight the connection between starch degradation and *de novo* FA biosynthesis in the considered setting. Finally, the bar plot in Fig. 9C shows the difference in deviation between data and model predictions for scenario 2 with respect to scenario 1 (*i.e.* scenario 2 – scenario 1) and demonstrates that scenario 1 better describes the observed FA biosynthesis rate than scenario 2. In summary, we can state that in all considered *in vitro* and *in silico* experiments, the model that allows for starch degradation into the system performed better than the model that does not allow for it. Altogether, these results provided very strong model-based evidence that starch degradation during the second stress response phase is a crucial mechanism to support continued FA synthesis.

**Carbon Redistribution from the TCA Cycle to FA Biosynthesis**—We then investigated the following question: Can the data-model integration support the hypothesis that malate from the TCA cycle (which is shown to increase by the metabolite data) is transported from the mitochondria to the chloroplast, where it is converted to CO<sub>2</sub> and pyruvate via ME? A positive answer would indicate that pyruvate can serve as a precursor for the chloroplast-based *de novo* FA synthesis. This

## Response of *H. pluvialis* Systems to Nitrogen Stress

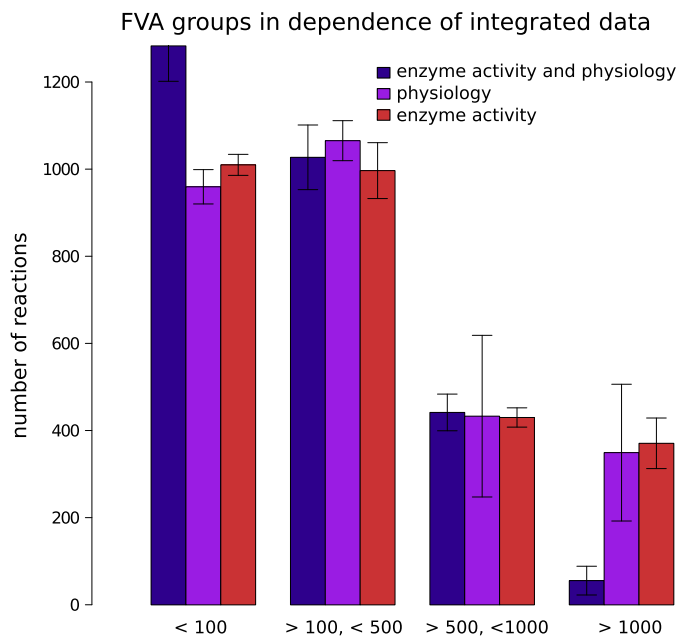


FIGURE 7. **Distribution of flux variability for experiment C.** Shown are the flux variabilities and S.D. values (error bars) for all reactions based on the integrated minimized discrepancy for three cases. The model is constrained by (i) enzymology and physiology data, (ii) enzymology data, and (iii) physiology data. The bar plots show four groups of reactions: low (<100 mmol g DW<sup>-1</sup> h<sup>-1</sup>), moderate (>100, <500 mmol g DW<sup>-1</sup> h<sup>-1</sup>), large (>500, <1000 mmol g DW<sup>-1</sup> h<sup>-1</sup>), and very large (>1000 mmol g DW<sup>-1</sup> h<sup>-1</sup>) variability.

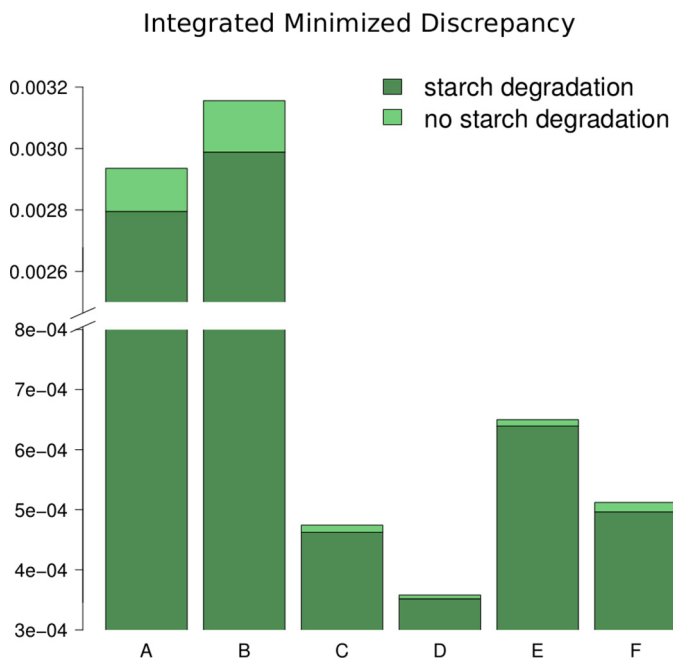
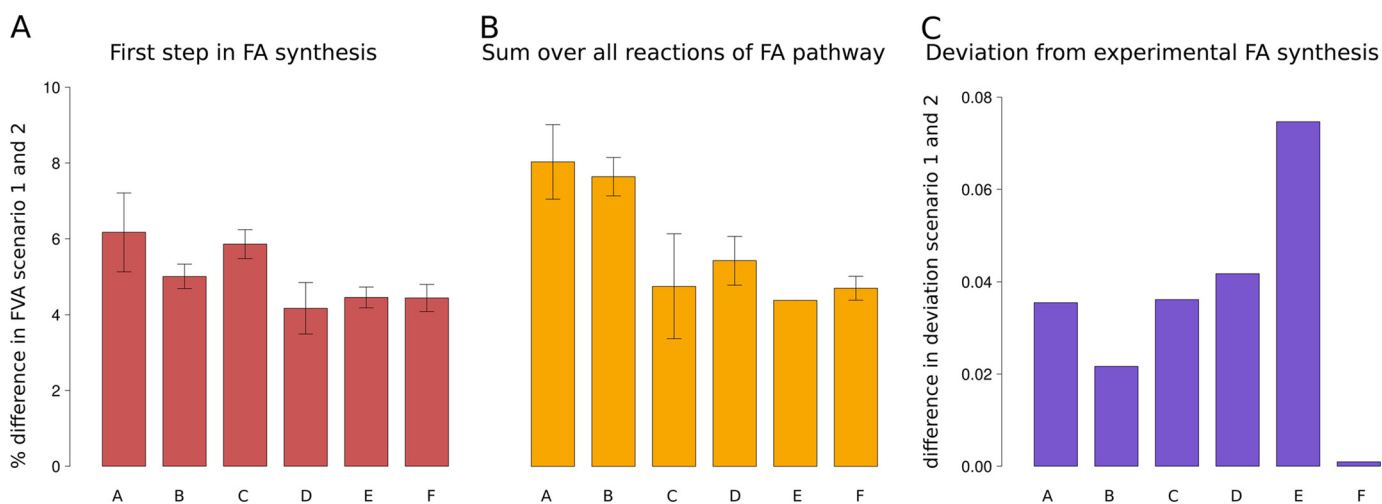


FIGURE 8. **Integrated minimized discrepancy for the model with and without starch degradation.** Given are the best values of the minimization between experimentally derived and predicted fluxes as the sum over the time course for all six experiments. *Dark green*, starch degradation into the system; *light green*, no starch degradation into the system. The model allowing for degradation performed 3.3% better, on average.

mechanism would support the fact that under nitrogen starvation and HL, TCA cycle activity increases to support a higher FA synthesis rate. To investigate this hypothesis, we made use of the predictions obtained from the InDisMinimizer and investigated the possible fluxes through the reactions involved

in the proposed mechanism. For the reactions of interest, we determined the range of allowed fluxes that result in the overall best data fit. The results of this flux variability analysis are shown in Fig. 10. The graphic illustrates the pathway from malate, originating from the TCA cycle, to carbon fixation and *de novo* FA biosynthesis in the chloroplast. The *numbers* represent the reactions involved. Their respective flux variability is given in the *left panel* of each reaction. Given are the average minimum and maximum flux values over all time points and all six experiments with their respective S.D. values. The mitochondrial and plastidial malate transporters can carry a flux of between 296.6 and 1440.9 and between 113.1 and 656.1 mmol g DW<sup>-1</sup> h<sup>-1</sup>, respectively. The three reactions involved in the conversion from malate to acetyl-CoA can carry a flux of between 0 and 729.3 mmol g DW<sup>-1</sup> h<sup>-1</sup> and allow for an overall flux into acetyl-CoA of 491.0 mmol g DW<sup>-1</sup> h<sup>-1</sup> (the sum of the smaller maximum flux value of reactions 3 and 4 and the maximum flux value of reaction 5, illustrated in Fig. 10). The flux into carbon fixation can range between 0 and 175.5 mmol g DW<sup>-1</sup> h<sup>-1</sup>, and the flux to malonyl-CoA, an initial step of FA biosynthesis, can range between 350.1 and 909.5 mmol g DW<sup>-1</sup> h<sup>-1</sup>. Taken together, these findings indicate that all of the involved reactions can form a high flux pathway and support the proposed mechanism of malate integration via pyruvate in the *de novo* synthesis of FA. However, because some reactions have a lower flux variability value of zero (reactions 3–6), just by considering the FVA results, we cannot rule out scenarios of flux distribution that carry a low flux through the described pathway.

To make statistical statements about the likelihood of a given reaction of the proposed pathway to carry a certain flux, we performed a flux distribution analysis that is based on a random flux sampling compatible with the derived flux bounds (from FVA). This novel approach, termed variability flux sampling, allows the prediction of flux values for the reactions of the pathway that are compliant with the imposed constraints (*e.g.* overall optimality of the flux solutions with respect to the InDisMinimizer, steady state) and minimize the Euclidian distance between the randomly chosen set of flux values and a set of feasible flux values for the respective reactions. The details of the computational approach are given under “Experimental Procedures.” The results of this analysis are depicted in Fig. 10 in the *right panel* of each reaction. The two malate transporters exhibit probability distributions for the fluxes that are centered below the middle of the respective FVA interval. Reaction 3 shows a nearly uniform distribution. Interestingly, for reactions 4 and 6 the determined distributions indicate that there is a low probability for a high flux from pyruvate to acetyl-CoA and from pyruvate to carbon fixation. Nevertheless, reaction 5 shows a bimodal distribution with one peak in the lower flux range ~50 mmol g DW<sup>-1</sup> h<sup>-1</sup>, whereas the other, higher peak is at ~300 mmol g DW<sup>-1</sup> h<sup>-1</sup>. Finally, the flux into fatty acid synthesis shows a probability distribution that is centered at ~900 mmol g DW<sup>-1</sup> h<sup>-1</sup>. Altogether, this analysis further supports the hypothesis of a high flux through the proposed pathway from malate to FA synthesis via reactions 1, 2, 5, and 7 and a high activity of malic enzyme. It furthermore suggests that pyruvate flux into acetyl-CoA and carbon fixations is low.



**FIGURE 9. Performance comparison for the model with and without starch degradation based on the integrated minimized discrepancy (best fit) for three different cases.** Shown are flux variability through the first reaction of *de novo* fatty acid biosynthesis (A) and the whole *de novo* fatty acid biosynthesis pathway (B) and respective S.D. values (error bars) for all time points. Shown is the percentage difference in variability for the solutions obtained for scenario 1 (degradation) and scenario 2 (no degradation). In both cases, scenario 1 shows a larger variability for all experiments. C, best minimized discrepancy for the fatty acid synthesis pathway, while accounting for the overall best fit. Shown is the difference between scenarios 1 and 2. Scenario 1 performed better for all experiments.

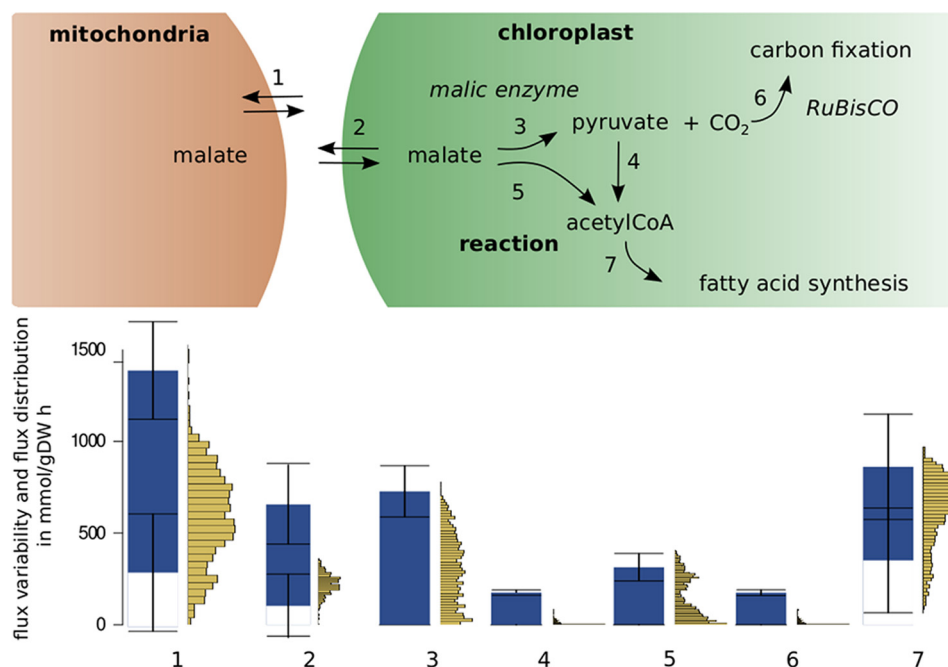


**FIGURE 10. Pathway representation and flux variability analysis of the proposed mechanism of carbon redistribution from the TCA cycle into *de novo* fatty acid biosynthesis.** Shown are the reactions involved in the carbon redistribution from mitochondrial malate to carbon fixation and fatty acid biosynthesis in the chloroplast. The reactions are numbered from 1 to 7. *Left panels* of each reaction, mean flux variability and S.D. value (error bars) over all time points and all experiments; *right panels*, probability distributions of flux values over all time points and all experiments.

These results put forward an interesting hypothesis for further experiments to investigate the role of chloroplastic ME in this chain of reactions and the fate of the pyruvate pool.

## DISCUSSION

*H. pluvialis* has been extensively investigated due to its ability to produce high amounts of the ketocarotenoid astaxanthin under inductive conditions that are mainly related to stress (8, 51). A large amount of research has been conducted to elucidate the astaxanthin biosynthesis pathway and its regulation (for reviews, see Refs. 51 and 52). Whereas the initial astaxanthin

synthesis utilizes the existing  $\beta$ -carotene as a precursor, bulk accumulation of astaxanthin esters will depend on *de novo*  $\beta$ -carotene synthesis (53). In fact, almost all of the genes involved in astaxanthin biosynthesis from isopentenyl pyrophosphate were found to be simultaneously up-regulated in transcriptional expression in high irradiance-induced red cells of *H. pluvialis* (54). Similarly, high expression levels of enzymes involved in the synthesis of terpenoids were also found in *Neochloris oleoabundans*, under nitrogen deficiency (55). In *Chlamydomonas reinhardtii*, light treatment was found to promote the accumulation of all transcripts of the methylerythritol

## Response of *H. pluvialis* Systems to Nitrogen Stress

phosphate pathway (56). Specifically in the current work, the fact that astaxanthin is accumulating to a level that is 30 times higher than the initial level of total carotenoids (Fig. 2) is a compelling indicator for *de novo* synthesis from the very early precursors and a rapid flow through those intermediates.

When exposed to different stresses, there is a positive correlation between the cellular content of FA and astaxanthin (4). However, FA accumulation is not dependent on astaxanthin synthesis (33), and as also shown for different algae (57), FA accumulation represents a more general stress response. Although some data on CH content under stress conditions can be found (6), only recently (12) was the dynamics of CH accumulation/degradation under stress targeted. This present study was aimed at elucidating the carbon partitioning in *H. pluvialis* under nitrogen starvation and HL stress; we therefore concentrated on the FAs and CHs, which together account for roughly 85% of the cell's biomass (Fig. 1). It is worth mentioning that astaxanthin content makes up a maximum of 4.5% of the biomass (8, 51) (Fig. 2A); thus, neither astaxanthin nor total carotenoid content contributes much to the understanding of carbon partitioning in *H. pluvialis*. Moreover, because astaxanthin accumulates as an FA ester, its small contribution is reflected in the FA content. To further deepen our understanding of carbon allocation in *H. pluvialis*, we employed metabolite and enzyme profiling to describe the physiological, metabolic, and enzymatic changes that accompany carbon repartitioning in *H. pluvialis* cells exposed to nitrogen starvation stress under HL. Moreover, we developed a putative model based on genome scale reconstruction of the model green alga *Chlamydomonas*, integrated two types of experimental data, and applied constraint-based optimization to predict flux distributions that reflect the experimental observations. We then used flux variability analysis to estimate the effects of the network and data constraints. Finally, two biological hypotheses were tested by considering alternative scenarios and comparing the predictive power. During the first 24 h of stress application, the cells responded by largely accumulating CH, accompanied by moderate FA accumulation. However, after 24 h of stress exposure, FA accumulation was accelerated, and TCH content decreased. Similar behavior has recently been shown in five different *Chlorellaceae* species, where lipid accumulation followed a reduction in stored starch when exposed to different stresses (13, 14). The hypothesis that during the second phase of the stress response (24–48 or 96 h), starch is degraded to support continuous FA synthesis was supported by our *in silico* experiments. We compared the computational results for two model scenarios, with and without starch degradation. The model that allowed for recycling of the building blocks resulting from the degradation process better described the experimental observations.

The present study also suggests a central role of the TCA cycle in FA biosynthesis upon stress application. Increased TCA cycle activity in the form of excess malate could support FA biosynthesis, assuming that the malate is transferred to the chloroplast, where it flows into FA synthesis. This flow has been previously reported in exponentially growing *C. reinhardtii* under heterotrophic conditions (58). Moreover, the CO<sub>2</sub> produced by this process could be fixed by Rubisco to increase photosynthetic capacity, as in C<sub>4</sub> plants. Both C<sub>4</sub> and C<sub>3</sub> pho-

tosynthetic pathways have been recently shown to coexist in the green tide-forming algae *Ulva prolifera* (59) and in different marine diatoms (60). Although we cannot confirm the existence of the C<sub>4</sub> pathway in *H. pluvialis*, the involvement of ME in its stress response (*i.e.* increases in CH and FA) was evident when using the ME inhibitor sesamol (12). Although the chloroplastic isoform of ME could not be measured, the proposed computational approaches strongly support both the hypothesis of a high flux route for malate via malate transport to the chloroplast with its subsequent conversion for *de novo* FA biosynthesis and a high activity of the malic enzyme. The low probabilities for a high flux from pyruvate to acetyl-CoA and carbon fixation suggest that pyruvate flows into other pathways. Pyruvate can serve as a precursor for the non-mevalonate 1-deoxy-D-xylulose-5-phosphate pathway for the biosynthesis of plastidic isoprenoids, such as carotenoids (61). Nevertheless, a high flux cannot be ruled out, as suggested by the FVA results. Finally, the predictions serve as a useful tool to investigate putative pathway fluxes; nevertheless, they have to be treated with care and could clearly be improved upon measurement of the chloroplastic malic enzyme.

The metabolite profiling led to the following observations. After 24 h of nitrogen starvation and HL stress, maltotriose, a starch degradation metabolite, decreased significantly, indicating a flow from starch toward glycolysis, which could in turn be used as a carbon skeleton for FA biosynthesis (62). Concomitantly, a large pool of glycerol, the backbone of TAG, was generated from the onset of stress exposure. This pool remained relatively large during the experiments, most likely to support TAG synthesis. Similarly, a correlation between starch breakdown and glycerol biosynthesis was recently shown to occur upon salt stress treatment in *Dunaliella tertiolecta* (63). Raffinose showed a pattern similar to that of the TCH, peaking after the first 12 h of stress exposure. This sugar has been suggested to be associated with stress tolerance, defense mechanisms, and carbon partitioning in the cell, serving as an antioxidant signaling stress (64). These observations indicate that as long as Chl content is relatively high (9–12 mg liter<sup>-1</sup>), the cell devotes its energy and carbon reserves to maintaining a carbon pool in the form of free sugars and starch. However, prolonged exposure to stress causes a shift toward starch degradation and FA synthesis (12). This behavior might also be related to the distinct pattern of the glycolytic enzymes phosphoenolpyruvate carboxylase, ME, and malate dehydrogenase, associated with pyruvate and downstream malate metabolism, observed throughout the experiment, namely reduced activity after 36 h. This characteristic could result from a cascade of events leading to the degradation of the photosynthetic apparatus (65) and enhanced FA synthesis. Moreover, these changes may be modulated by key enzymes, such as phosphoenolpyruvate carboxylase and pyruvate kinase, which are, in turn, regulated by TCA cycle intermediates (66, 67). However, a more comprehensive study would be needed to confirm this hypothesis.

When *H. pluvialis* is subjected to environmental stress, reactive oxygen species are produced (8). The generation of reactive oxygen species activates the synthesis of astaxanthin, which protects the cell by shielding it from excessive irradiation (68). However, reactive oxygen species are also known to inhibit the

TCA cycle enzymes 2-oxoglutarate dehydrogenase and succinyl-CoA synthetase, thereby shuttling 2-oxoglutarate toward the GABA shunt (69–72). In the present study, we found further evidence for this alternative route (*i.e.* the accumulation of GABA). This non-protein amino acid is known to be regulated by enhanced glutamate decarboxylase activity via  $\text{Ca}^{2+}$ -calmodulin and reduced succinyl semialdehyde dehydrogenase activity as a response to altered energy balance and redox status (73). Among the different roles suggested for the GABA shunt (74–77), it has been proposed as a modulator of the carbon-nitrogen balance (78). We suggest that in *H. pluvialis* under nitrogen starvation and HL, reduced nitrogen derived from the deamination of free amino acids in the cell is stored in the GABA pool, which can be used as a buffer for the turnover of internal proteins. This suggestion is further supported by results obtained from *C. reinhardtii* under ammonium deficiency (24); TCA cycle enzyme activity increased, potentially providing carbon skeletons for amino acid metabolism. It has been shown that certain proteins in *H. pluvialis* degrade under nitrogen starvation, whereas others are actually built (8, 79–81). Therefore, although volumetric protein content is preserved, it is likely that there is a change in the protein profile.

Finally, our findings demonstrate that physiological, metabolite, and enzyme activity data in combination with constraint-based optimization approaches can be used to test biological hypotheses. The combination of experimental data and large scale networks has two advantages. On the one hand, integrating (time-resolved) experimental data enables the formulation of more realistic constraints on the model than those stemming only from biochemistry, thermodynamics, and model-based boundaries (30). On the other hand, the network framework allows the capture of interdependencies between reactions, which would not be revealed by a simple analysis of the experimental data. By following this approach, we provide model-driven evidence that starch degradation during the second phase of the stress response supports continued FA synthesis. Moreover, we found support for malate integration in the *de novo* synthesis of FA, although precise claims regarding this hypothesis require more direct experimental validation.

## REFERENCES

- Amin, S. (2009) Review on biofuel oil and gas production processes from microalgae. *Energy Conversion and Management*. **50**, 1834–1840
- Rosenberg, J. N., Oyler, G. A., Wilkinson, L., and Betenbaugh, M. J. (2008) A green light for engineered algae: redirecting metabolism to fuel a biotechnology revolution. *Curr. Opin. Biotechnol.* **19**, 430–436
- Siaut, M., Cuiné, S., Cagnon, C., Fessler, B., Nguyen, M., Carrier, P., Beyly, A., Beisson, F., Triantaphylidès, C., and Li-Beisson, Y. (2011) Oil accumulation in the model green alga *Chlamydomonas reinhardtii*: characterization, variability between common laboratory strains and relationship with starch reserves. *BMC Biotechnol.* **11**, 7
- Zhekisheva, M., Boussiba, S., Khozin-Goldberg, I., Zarka, A., and Cohen, Z. (2002) Accumulation of oleic acid in *Haematococcus pluvialis* (Chlorophyceae) under nitrogen starvation or high light is correlated with that of astaxanthin. *J. Phycol.* **38**, 325–331
- Rabbani, S., Beyer, P., Lintig, J., Huguency, P., and Kleinig, H. (1998) Induced  $\beta$ -carotene synthesis driven by triacylglycerol deposition in the unicellular alga *Dunaliella bardawil*. *Plant Physiol.* **116**, 1239–1248
- Boussiba, S., and Vonshak, A. (1991) Astaxanthin accumulation in the green alga *Haematococcus pluvialis*. *Plant Cell Physiol.* **32**, 1077–1082
- Spolaore, P., Joannis-Cassan, C., Duran, E., and Isambert, A. (2006) Commercial applications of microalgae. *J. Biosci. Bioeng.* **101**, 87–96
- Boussiba, S. (2000) Carotenogenesis in the green alga *Haematococcus pluvialis*: cellular physiology and stress response. *Physiol. Plant.* **108**, 111–117
- Borowitzka, M. A., Huisman, J. M., and Osborn, A. (1991) Culture of the astaxanthin-producing green alga *Haematococcus pluvialis*: effects of nutrients on growth and cell type. *J. Appl. Phycol.* **3**, 295–304
- Aflalo, C., Meshulam, Y., Zarka, A., and Boussiba, S. (2007) On the relative efficiency of two- vs. one-stage production of astaxanthin by the green alga: *Haematococcus pluvialis*. *Biotechnol. Bioeng.* **98**, 300–305
- Boussiba, S., Bing, W., Yuan, J., Zarka, A., and Chen, F. (1999) Changes in pigments profile in the green alga *Haematococcus pluvialis* exposed to environmental stresses. *Biotechnol. Lett.* **21**, 601–604
- Recht, L., Zarka, A., and Boussiba, S. (2012) Patterns of carbohydrate and fatty acid changes under nitrogen starvation in the microalgae *Haematococcus pluvialis* and *Nannochloropsis* sp. *Appl. Microbiol. Biotechnol.* **94**, 1495–1503
- Mizuno, Y., Sato, A., Watanabe, K., Hirata, A., Takeshita, T., Ota, S., Sato, N., Zachleder, V., Tsuzuki, M., and Kawano, S. (2013) Sequential accumulation of starch and lipid induced by sulfur deficiency in *Chlorella* and *Parachlorella* species. *Bioresour. Technol.* **129**, 150–155
- Goncalves, E. C., Johnson, J. V., and Rathinasabapathi, B. (2013) Conversion of membrane lipid acyl groups to triacylglycerol and formation of lipid bodies upon nitrogen starvation in biofuel green algae *Chlorella* UTEX29. *Planta* **238**, 895–906
- Sirevåg, R., and Levine, R. P. (1972) Fatty acid synthetase from *Chlamydomonas reinhardtii* sites of transcription and translation. *J. Biol. Chem.* **247**, 2586–2591
- Rawsthorne, S. (2002) Carbon flux and fatty acid synthesis in plants. *Prog. Lipid Res.* **41**, 182–196
- Radakovits, R., Jinkerson, R. E., Darzins, A., and Posewitz, M. C. (2010) Genetic engineering of algae for enhanced biofuel production. *Eukaryot. Cell* **9**, 486–501
- Courchesne, N. M., Parisien, A., Wang, B., and Lan, C. Q. (2009) Enhancement of lipid production using biochemical, genetic and transcription factor engineering approaches. *J. Biotechnol.* **141**, 31–41
- Hu, Q., Sommerfeld, M., Jarvis, E., Ghirardi, M., Posewitz, M., Seibert, M., and Darzins, A. (2008) Microalgal triacylglycerols as feedstocks for biofuel production: perspectives and advances. *Plant J.* **54**, 621–639
- Beer, L. L., Boyd, E. S., Peters, J. W., and Posewitz, M. C. (2009) Engineering algae for biohydrogen and biofuel production. *Curr. Opin. Biotechnol.* **20**, 264–271
- Li, Y., Han, D., Hu, G., Dauvillee, D., Sommerfeld, M., Ball, S., and Hu, Q. (2010) *Chlamydomonas* starchless mutant defective in ADP-glucose pyrophosphorylase hyper-accumulates triacylglycerol. *Metab. Eng.* **12**, 387–391
- Sweetlove, L. J., Beard, K. F., Nunes-Nesi, A., Fernie, A. R., and Ratcliffe, R. G. (2010) Not just a circle: flux modes in the plant TCA cycle. *Trends Plant Sci.* **15**, 462–470
- Lee do, Y., Park, J. J., Barupal, D. K., and Fiehn, O. (2012) System response of metabolic networks in *Chlamydomonas reinhardtii* to total available ammonium. *Mol. Cell. Proteomics* **11**, 973–988
- Hockin, N. L., Mock, T., Mulholland, F., Kopriva, S., and Malin, G. (2012) The response of diatom central carbon metabolism to nitrogen starvation is different from that of green algae and higher plants. *Plant Physiol.* **158**, 299–312
- Kim, D., Hong, S., Bae, J., Yim, N., Jin, E., and Lee, C. (2011) Transcriptomic analysis of *Haematococcus lacustris* during astaxanthin accumulation under high irradiance and nutrient starvation. *Biotechnol. Bioprocess Eng.* **16**, 698–705
- Araújo, W. L., Nunes-Nesi, A., Nikoloski, Z., Sweetlove, L. J., and Fernie, A. R. (2012) Metabolic control and regulation of the tricarboxylic acid cycle in photosynthetic and heterotrophic plant tissues. *Plant Cell Environ.* **35**, 1–21
- Gibon, Y., Blaessing, O. E., Hannemann, J., Carillo, P., Höhne, M., Hendriks, J. H., Palacios, N., Cross, J., Selbig, J., and Stitt, M. (2004) A robot-based platform to measure multiple enzyme activities in *Arabidopsis* using a set of cycling assays: comparison of changes of enzyme activities and

## Response of *H. pluvialis* Systems to Nitrogen Stress

- transcript levels during diurnal cycles and in prolonged darkness. *Plant Cell* **16**, 3304–3325
28. Xiong, W., Liu, L., Wu, C., Yang, C., and Wu, Q. (2010) <sup>13</sup>C-tracer and gas chromatography-mass spectrometry analyses reveal metabolic flux distribution in the oleaginous microalga *Chlorella protothecoides*. *Plant Physiol.* **154**, 1001–1011
29. Wienkoop, S., Weiss, J., May, P., Kempa, S., Irgang, S., Recuenco-Munoz, L., Pietzke, M., Schwemmer, T., Rupprecht, J., and Egelhofer, V. (2010) Targeted proteomics for *Chlamydomonas reinhardtii* combined with rapid subcellular protein fractionation, metabolomics and metabolic flux analyses. *Mol. Biosyst.* **6**, 1018–1031
30. Lewis, N. E., Nagarajan, H., and Palsson, B. O. (2012) Constraining the metabolic genotype-phenotype relationship using a phylogeny of *in silico* methods. *Nat. Rev. Microbiol.* **10**, 291–305
31. Orth, J. D., Thiele, I., and Palsson, B. Ø. (2010) What is flux balance analysis?. *Nat. Biotechnol.* **28**, 245–248
32. Stanier, R. Y., Kunisawa, R., Mandel, M., and Cohen-Bazire, G. (1971) Purification and properties of unicellular blue-green algae (order Chroococcales). *Bacteriol. Rev.* **35**, 171–205
33. Zhekisheva, M., Zarka, A., Khozin-Goldberg, I., Cohen, Z., and Boussiba, S. (2005) Inhibition of astaxanthin synthesis under high irradiance does not abolish triacylglycerol accumulation in the green alga *Haematococcus pluvialis* (Chlorophyceae). *J. Phycol.* **41**, 819–826
34. Smith, P. K., Krohn, R. I., Hermanson, G. T., Mallia, A. K., Gartner, F. H., Provenzano, M. D., Fujimoto, E. K., Goeke, N. M., Olson, B. J., and Klenk, D. C. (1985) Measurement of protein using bicinchoninic acid. *Anal. Biochem.* **150**, 76–85
35. Roe, J. H. (1955) The determination of sugar in blood and spinal fluid with anthrone reagent. *J. Biol. Chem.* **212**, 335–343
36. Hewitt, B. R. (1958) Spectrophotometric determination of total carbohydrate. *Nature* **182**, 246–247
37. Gibon, Y., Pyl, E. T., Sulpice, R., Lunn, J. E., Höhne, M., Günther, M., and Stitt, M. (2009) Adjustment of growth, starch turnover, protein content and central metabolism to a decrease of the carbon supply when *Arabidopsis* is grown in very short photoperiods. *Plant Cell Environ.* **32**, 859–874
38. Nunes-Nesi, A., Carrari, F., Gibon, Y., Sulpice, R., Lytvochenko, A., Fisahn, J., Graham, J., Ratcliffe, R. G., Sweetlove, L. J., and Fernie, A. R. (2007) Deficiency of mitochondrial fumarate hydratase activity in tomato plants impairs photosynthesis via an effect on stomatal function. *Plant J.* **50**, 1093–1106
39. Piques, M., Schulze, W. X., Höhne, M., Usadel, B., Gibon, Y., Rohwer, J., and Stitt, M. (2009) Ribosome and transcript copy numbers, polysome occupancy and enzyme dynamics in *Arabidopsis*. *Mol. Syst. Biol.* **5**, 314
40. Wheeler, M. C., Tronconi, M. A., Drincovich, M. F., Andreo, C. S., Flügge, U. I., and Maurino, V. G. (2005) A comprehensive analysis of the NADP-malic enzyme gene family of *Arabidopsis*. *Plant Physiol.* **139**, 39–51
41. Lisec, J., Schauer, N., Kopka, J., Willmitzer, L., and Fernie, A. R. (2006) Gas chromatography mass spectrometry-based metabolite profiling in plants. *Nat. Protoc.* **1**, 387–396
42. Luedemann, A., Strassburg, K., Erban, A., and Kopka, J. (2008) TagFinder for the quantitative analysis of gas chromatography–mass spectrometry (GC-MS)-based metabolite profiling experiments. *Bioinformatics* **24**, 732–737
43. Erban, A., Schauer, N., Fernie, A. R., and Kopka, J. (2007) Nonsupervised construction and application of mass spectral and retention time index libraries from time-of-flight gas chromatography-mass spectrometry metabolite profiles. *Methods Mol. Biol.* **358**, 19–38
44. Reynolds, A. P., Richards, G., de la Iglesia, B., and Rayward-Smith, V. J. (2006) Clustering rules: a comparison of partitioning and hierarchical clustering algorithms. *Journal of Mathematical Modelling and Algorithms* **5**, 475–504
45. Chang, R. L., Ghamsari, L., Manichaikul, A., Hom, E. F., Balaji, S., Fu, W., Shen, Y., Hao, T., Palsson, B. Ø., and Salehi-Ashtiani, K. (2011) Metabolic network reconstruction of *Chlamydomonas* offers insight into light-driven algal metabolism. *Mol. Syst. Biol.* **7**, 518
46. Fan, L., Vonshak, A., Zarka, A., and Boussiba, S. (1998) Does astaxanthin protect *Haematococcus* against light damage?. *Z. Naturforsch. C* **53**, 93–100
47. Heinrich, R., and Schuster, S. (1996) *The Regulation of Cellular Systems*. Chapman & Hall, New York
48. Mahadevan, R., and Schilling, C. (2003) The effects of alternate optimal solutions in constraint-based genome-scale metabolic models. *Metab. Eng.* **5**, 264–276
49. Fait, A., and Fernie, A. R. (2009) Data integration. in *Plant Metabolic Networks* (Schwender, J., ed), Springer, NY
50. Caspi, R., Altman, T., Dreher, K., Fulcher, C. A., Subhraveti, P., Keseler, I. M., Kothari, A., Krummenacker, M., Latendresse, M., and Mueller, L. A. (2012) The MetaCyc database of metabolic pathways and enzymes and the BioCyc collection of pathway/genome databases. *Nucleic Acids Res.* **40**, D742–D753
51. Lemoine, Y., and Schoefs, B. (2010) Secondary ketocarotenoid astaxanthin biosynthesis in algae: a multifunctional response to stress. *Photosynth. Res.* **106**, 155–177
52. Han, D., Li, Y., and Hu, Q. (2013) Astaxanthin in microalgae: pathways, functions and biotechnological implications. *Algae* **28**, 131–147
53. Schoefs, B., Rmiki, N., Rachadi, J., and Lemoine, Y. (2001) Astaxanthin accumulation in *Haematococcus* requires a cytochrome P450 hydroxylase and an active synthesis of fatty acids. *FEBS Lett.* **500**, 125–128
54. Gwak, Y., Hwang, Y. S., Wang, B., Kim, M., Jeong, J., Lee, C. G., Hu, Q., Han, D., and Jin, E. (2014) Comparative analyses of lipidomes and transcriptomes reveal a concerted action of multiple defensive systems against photooxidative stress in *Haematococcus pluvialis*. *J. Exp. Bot.* **65**, 4317–4334
55. Rismani-Yazdi, H., Haznedaroglu, B. Z., Hsin, C., and Peccia, J. (2012) Transcriptomic analysis of the oleaginous microalga *Neochloris oleoabundans* reveals metabolic insights into triacylglyceride accumulation. *Bio-technol. Biofuels* **5**, 74
56. Sun, T. H., Liu, C. Q., Hui, Y. Y., Wu, W. K., Zhou, Z. G., and Lu, S. (2010) Coordinated regulation of gene expression for carotenoid metabolism in *Chlamydomonas reinhardtii*. *J. Integrative Plant Biol.* **52**, 868–878
57. Roessner, U., Luedemann, A., Brust, D., Fiehn, O., Linke, T., Willmitzer, L., and Fernie, A. (2001) Metabolic profiling allows comprehensive phenotyping of genetically or environmentally modified plant systems. *Plant Cell* **13**, 11–29
58. Boyle, N. R., and Morgan, J. A. (2009) Flux balance analysis of primary metabolism in *Chlamydomonas reinhardtii*. *BMC Syst. Biol.* **3**, 4
59. Xu, J., Fan, X., Zhang, X., Xu, D., Mou, S., Cao, S., Zheng, Z., Miao, J., and Ye, N. (2012) Evidence of coexistence of C3 and C4 photosynthetic pathways in a green-tide-forming alga, *Ulva prolifera*. *PLoS One* **7**, e37438
60. Obata, T., Fernie, A. R., and Nunes-Nesi, A. (2013) The central carbon and energy metabolism of marine diatoms. *Metabolites* **3**, 325–346
61. Lichtenthaler, H. K. (1999) The 1-deoxy-D-xylulose-5-phosphate pathway of isoprenoid biosynthesis in plants. *Annu. Rev. Plant Physiol. Plant Mol. Biol.* **50**, 47–65
62. Paunier, L., and Favarger, P. (1960) Synthesis of fats from acetate or glucose. 9. Transformation of glucose into fatty acids by oxidation in the mouse *in vivo*. *Helv. Chim. Acta* **43**, 118–129
63. Goyal, A. (2007) Osmoregulation in *Dunaliella*, Part II: photosynthesis and starch carbon for glycerol synthesis during a salt stress in *Dunaliella tertiolecta*. *Plant Physiol. Biochem.* **45**, 705–710
64. ElSayed, A., Rafudeen, M., and Golldack, D. (2013) Physiological aspects of raffinose family oligosaccharides in plants: protection against abiotic stress. *Plant Biol.* **10.1111/plb.12053**
65. Berges, J. A., Charlebois, D. O., Mauzerall, D. C., and Falkowski, P. G. (1996) Differential effects of nitrogen limitation on photosynthetic efficiency of photosystems I and II in microalgae. *Plant Physiol.* **110**, 689–696
66. Chollet, R., Vidal, J., and O’Leary, M. H. (1996) Phosphoenolpyruvate carboxylase: a ubiquitous, highly regulated enzyme in plants. *Annu. Rev. Plant Physiol. Plant Mol. Biol.* **47**, 273–298
67. Duggleby, R. G., and Dennis, D. T. (1973) Pyruvate kinase, a possible regulatory enzyme in higher plants. *Plant Physiol.* **52**, 312–317
68. Yong, Y. Y. R., and Lee, Y.-K. (1991) Do carotenoids play a photoprotective role in the cytoplasm of *Haematococcus lacustris* (Chlorophyta)?. *Phycologia* **30**, 257–261
69. Sweetlove, L. J., Heazlewood, J. L., Herald, V., Holtzapffel, R., Day, D. A., Leaver, C. J., and Millar, A. H. (2002) The impact of oxidative stress on *Arabidopsis* mitochondria. *Plant J.* **32**, 891–904
70. Studart-Guimãraes, C., Fait, A., Nunes-Nesi, A., Carrari, F., Usadel, B., and

- Fernie, A. R. (2007) Reduced expression of succinyl-coenzyme A ligase can be compensated for by up-regulation of the  $\gamma$ -aminobutyrate shunt in illuminated tomato leaves. *Plant Physiol.* **145**, 626–639
71. Bolton, M. D. (2009) Primary metabolism and plant defense-fuel for the fire. *Mol. Plant Microbe Interact.* **22**, 487–497
  72. Bown, A. W., and Shelp, B. J. (1997) The metabolism and functions of  $\gamma$ -aminobutyric acid. *Plant Physiol.* **115**, 1–5
  73. Bouché, N., Fait, A., Zik, M., and Fromm, H. (2004) The root-specific glutamate decarboxylase (GAD1) is essential for sustaining GABA levels in *Arabidopsis*. *Plant Mol. Biol.* **55**, 315–325
  74. Bouché, N., Fait, A., Bouchez, D., Møller, S. G., and Fromm, H. (2003) Mitochondrial succinic-semialdehyde dehydrogenase of the  $\gamma$ -aminobutyrate shunt is required to restrict levels of reactive oxygen intermediates in plants. *Proc. Natl. Acad. Sci.* **100**, 6843–6848
  75. Shelp, B. J., Bown, A. W., and McLean, M. D. (1999) Metabolism and functions of  $\gamma$ -aminobutyric acid. *Trends Plant Sci.* **4**, 446–452
  76. Ma, Z., Richard, H., Tucker, D. L., Conway, T., and Foster, J. W. (2002) Collaborative regulation of *Escherichia coli* glutamate-dependent acid resistance by two AraC-like regulators, GadX and GadW (YhiW). *J. Bacteriol.* **184**, 7001–7012
  77. Bouché, N., Lacombe, B., and Fromm, H. (2003) GABA signaling: a conserved and ubiquitous mechanism. *Trends Cell Biol.* **13**, 607–610
  78. Fait, A., Fromm, H., Walter, D., Galili, G., and Fernie, A. R. (2008) Highway or byway: the metabolic role of the GABA shunt in plants. *Trends Plant Sci.* **13**, 14–19
  79. Tan, S., Cunningham, F. X., Youmans, M., Grabowski, B., Sun, Z., and Gantt, E. (1995) Cytochrome f loss in astaxanthin accumulating red cells of *Haematococcus pluvialis* (Chlorophyceae): comparison of photosynthetic activity, photosynthetic enzymes, and thylakoid membrane polypeptides in red and green cells. *J. Phycol.* **31**, 897–905
  80. Wang, S. B., Chen, F., Sommerfeld, M., and Hu, Q. (2004) Proteomic analysis of molecular response to oxidative stress by the green alga *Haematococcus pluvialis* (Chlorophyceae). *Planta* **220**, 17–29
  81. Peled, E., Leu, S., Zarka, A., Weiss, M., Pick, U., Khozin-Goldberg, I., and Boussiba, S. (2011) Isolation of a novel oil globule protein from the green alga *Haematococcus pluvialis* (Chlorophyceae). *Lipids* **46**, 851–861

**Metabolite Profiling and Integrative Modeling Reveal Metabolic Constraints for Carbon Partitioning under Nitrogen Starvation in the Green Algae *Haematococcus pluvialis***

Lee Recht, Nadine Töpfer, Albert Batushansky, Noga Sikron, Yves Gibon, Aaron Fait, Zoran Nikoloski, Sammy Boussiba and Aliza Zarka

*J. Biol. Chem.* 2014, 289:30387-30403.

doi: 10.1074/jbc.M114.555144 originally published online September 2, 2014

---

Access the most updated version of this article at doi: [10.1074/jbc.M114.555144](https://doi.org/10.1074/jbc.M114.555144)

Alerts:

- [When this article is cited](#)
- [When a correction for this article is posted](#)

[Click here](#) to choose from all of JBC's e-mail alerts

Supplemental material:

<http://www.jbc.org/content/suppl/2014/09/02/M114.555144.DC1>

This article cites 79 references, 16 of which can be accessed free at <http://www.jbc.org/content/289/44/30387.full.html#ref-list-1>